Journal of CO2 Utilization 101 (2025) 103222

Contents lists available at ScienceDirect

Journal of CO2 Utilization

journal homepage: www.elsevier.com/locate/jcou

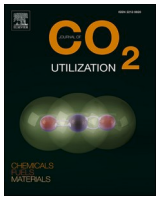

Green copper oxide photocathodes using plant extracts for an efficient photoelectrochemical CO_2 conversion to alcohols

Amena Mrabet [a,*], Ivan Merino-Garcia [b], Maite Perfecto-Irigaray [c,d], Garikoitz Beobide [c], Mohamed Khaddor [a], Jonathan Albo [b,*]

[a] Laboratory of Physical Chemistry of Materials, Natural Substances and Environment (LAMSE), Chemistry Department, Faculty of Sciences and Techniques of Tangier, B.P. 416, Tangier 90000, Morocco
[b] Departamento de Ingenierías Química y Biomolecular, Universidad de Cantabria, Avenida de los Castros s/n, Santander 39005, Spain
[c] Department of Organic and Inorganic Chemistry, University of the Basque Country, UPV/EHU, P.O. 644, Bilbao E-48080, Spain
[d] ISIS Neutron and Muon Source, STFC Rutherford Appleton Laboratory, Didcot OX11 0QX, UK

ARTICLE INFO

Keywords:
Green synthesized CuO NPs
Plant extracts
CO_2 photoelectroreduction
Photocathodes
Alcohols

ABSTRACT

In this study, green home-made synthesized copper oxide (CuO) nanoparticles are employed as photocathodes in the form of gas diffusion electrodes (GDEs) for the continuous photoelectrochemical (PEC) conversion of CO_2 into valuable products, including methanol and ethanol. CuO nanoparticles synthesized using plant extracts from *Salvia rosmarinus* (CuO-R), *Laurus nobilis* (CuO-L), and *Origanum vulgare* (CuO-O) are prepared in a green, sustainable manner, leveraging the phytochemicals in these plants for nanoparticle formation and stabilization. The eco-friendly synthesized CuO-based photocathodes are then prepared by an automated spray pyrolysis deposition technique and comprehensively physico-chemically, optically, and photoelectrochemically characterized, revealing enhanced photocurrent densities and promising product selectivity for CO_2 reduction to alcohols under visible light irradiation. Among the eco-synthesized photocathodes, CuO-R exhibited the highest PEC activity, achieving a Faradaic efficiency exceeding 66 % for methanol, with an energy efficiency of 39.2 %, while requiring a minimized external potential of −0.37 V (vs. RHE), lower than that for the chemically synthesized catalyst (CuO-P). Post-reaction analysis further confirmed that CuO-R maintained its structural integrity after continuous operation, reinforcing its superior stability and PEC efficiency. These results demonstrate that green synthesis pathways provide a sustainable and efficient approach to developing high-performance photocathodes for PEC CO_2 reduction, offering promising potential for scalable solar-driven carbon conversion technologies.

1. Introduction

Escalating levels of CO_2 in the atmosphere caused by human activities is a significant challenge nowadays due to their contribution to global warming and environmental instability [1,2]. To address these issues, various strategies have been proposed, including the use of carbon capture, storage and utilization (CCSU) technologies, sustainable agricultural practices, and the adoption of sustainable energy sources. Among them, the conversion of captured CO_2 into valuable products, which offers a dual solution of reducing emissions and promoting sustainable energy production in the form of chemical bonds, emerges as a sustainable solution for climate change mitigation and energy generation alternatives [3,4]. However, several challenges must be addressed before the commercialization of CO_2 conversion technologies, including overall energy consumption or catalyst stability, among others [5].

Although the electrochemical (EC) conversion of CO_2 to value-added products has been widely studied in literature, it suffers from several critical bottlenecks that limit its commercial viability. One of the primary challenges is the high energy demand, as the CO_2 molecule is highly stable, requiring significant overpotentials to drive the reduction reaction. This often necessitates substantial external energy input, as the reaction requires more energy to proceed than is retained in the resulting products [6]. However, photoelectrochemical (PEC) systems offer a potentially more sustainable alternative by harnessing sunlight as an energy source, which can lower energy requirements compared to conventional EC approaches [7–9]. The challenges of poor selectivity in EC and PEC processes for CO_2 conversion, however, significantly complicate the production of desired products. Both methods often yield

* Corresponding authors.
E-mail addresses: amena.mrabet@etu.uae.ac.ma (A. Mrabet), alboj@unican.es (J. Albo).

https://doi.org/10.1016/j.jcou.2025.103222
Received 16 June 2025; Received in revised form 29 July 2025; Accepted 11 September 2025
Available online 18 September 2025

a mixture of byproducts, necessitating complex and costly separation. Besides, the competition between the hydrogen evolution reaction (HER) and CO_2 reduction further complicates product selectivity [10,11]. By leveraging sunlight in PEC processes, energy requirements can be minimized, potentially reducing HER interference and enhancing selectivity for CO_2 conversion products [12]. Moreover, catalyst stability is a major concern, as many catalysts degrade over time due to harsh reaction conditions, leading to a decrease in performance and the need for their frequent replacement or regeneration [13,14].

PEC systems can be configured in different ways, including tandem or single-cell setups, each with unique advantages for CO_2 reduction. Among these configurations, the photocathode/dark anode setup is particularly promising [15]. In this configuration, the photocathode harnesses sunlight to drive CO_2 reduction, while the dark anode facilitates oxidation reactions, offering a simplified design and reduced energy requirements by selectively targeting the reduction of CO_2 on the photocathode side. The challenge of simultaneous CO_2 reduction and light absorption on the same surface in PEC systems can significantly hinder reaction efficiency due to competition between these processes. Addressing this issue involves innovative strategies in photocatalyst design and interface engineering to optimize process performance [16]. Efficient photocathodes are not only critical for light absorption, but also for promoting selective CO_2 conversion into specific fuels, while minimizing the production of undesired byproducts [17]. Current research has been focused on improving the performance of photocathode materials by enhancing their efficiency, selectivity, and stability to enable practical, large-scale PEC technology implementation [18]. Various materials, such as TiO_2 and copper oxides have been explored for achieving high photocurrent densities and improved product selectivity towards valuable CO_2 reduction products like methanol, ethanol, or formate [19–21]. Additionally, advancements in non-noble metal catalysts and photovoltaics-assisted PEC systems have contributed to overcoming the efficiency limitations and cost barriers for practical PEC CO_2 reduction [22]. Among the possible materials, CuO represents a promising photocathode material for PEC applications due to its favorable band structure, abundance, low cost, and stability under PEC conditions [23,24]. CuO nanoparticles offer high surface-to-volume ratios, tunable characteristics, and enhanced catalytic activity, improving the performance of photocathodes in CO_2 reduction reactions [25]. Additionally, its broad visible light absorption spectrum makes it well-suited material for solar-powered devices [24]. To optimize the structural, optical, and electrochemical properties of CuO photocathodes, precise control over their synthesis is crucial for achieving an efficient performance [26]. By carefully tailoring the synthesis methods and conditions, CuO photocathodes can be engineered to maximize their effectiveness in various PEC applications [27,28].

While various materials and synthesis strategies, such as hydrothermal methods [29], sol-gel synthesis, and electrodeposition [30], have been explored to enhance the performance of photocathodes for PEC CO_2 reduction, the development of eco-friendly and sustainable synthesis methods still remains underexplored [31,32]. Green synthesized CuO nanoparticles have already shown promise in a wide number of applications, such as photocatalytic industrial dye degradation and antibacterial activity [33–35]. However, their use in photo-assisted CO_2 conversion remains largely unexplored, and this study seeks to investigate this application for the first time, as far as the authors know. Previous studies have shown that green synthesized nanoparticles have higher stability and catalytic activity, both of which are essential for PEC systems to function properly in the long term [36]. The application of extracts from *Salvia rosmarinus*, *Laurus nobilis*, and *Origanum vulgare* specifically takes advantage of their distinct phytochemical profiles, which could give the CuO NPs additional advantageous characteristics. In the green synthesis process, electron absorption and donation from plant extracts leads to the reduction of copper ions, which encourages nanoparticle formation [37]. Reactive plant chemicals then induce oxidation and a tertiary coating, stabilizing the nanoparticles and avoiding agglomeration [38]. For example, *Salvia rosmarinus* contains rosmarinic acid and diterpenes, which prevent nanoparticle aggregation and increase their reactivity [39,40], while *Laurus nobilis* contributes tannins and essential oils that enhance nanoparticle stability [41,42]. *Origanum vulgare*, rich in thymol and carvacrol, further stabilizes the nanoparticles and may enhance their catalytic activity [43,44].

In this study, we introduce a novel application of green synthesized CuO NPs as photocathodes in PEC systems, utilizing plant extracts such as *Salvia rosmarinus*, *Laurus nobilis*, and *Origanum vulgare* to achieve tunable properties, offering a sustainable and effective alternative to traditional synthesis routes [45]. The key point in this study is the use of these eco-friendly synthesis techniques, leveraging the natural reducing agents and stabilizers found in the plant extracts to evaluate the catalytic activity and stability of the synthesized CuO catalysts as photocathodes for the continuous conversion of CO_2 to alcohols under visible light irradiation [46–48]. This method aligns with the principles of green chemistry, eliminating the use of hazardous chemicals, reducing environmental impact, and improving scalability [49,50].

In pursuing this research, our goal is to drive innovation in sustainable materials for renewable energy applications and contribute to global efforts to mitigate CO_2 emissions and promote the transition to a circular economy. By demonstrating the efficacy and sustainability of CuO photocathodes synthesized using plant extracts, we hope to pave the way for more eco-friendly and efficient PEC systems for CO_2 reduction.

2. Materials and methods

2.1. Synthesis of CuO nanoparticles

Chemical synthesis:

A 200 mL 1 M aqueous solution of copper(II) sulphate pentahydrate ($CuSO_4$, $5H_2O$, Sigma-Aldrich, >99 % purity) is prepared for the chemical production of CuO NPs, and it is placed on a hot plate preheated to 70°C. The copper sulphate solution is then vigorously stirred and dropped wise mixed with a 200 mL 2 M aqueous solution of sodium hydroxide (NaOH) until pH reaches 6–7. Immediately, a significant amount of black precipitate formed. After centrifuging the precipitate, distilled water is used to wash it three times. To increase purity, the resultant copper oxide nanoparticles are dried and then annealed for two hours at 450 °C in an air furnace following a previously reported procedure [51].

2.2. Plant-extract mediated synthesis

In brief, 20 g of dried leaf powder from *Salvia rosmarinus*, *Laurus nobilis*, and *Origanum vulgare*, sourced from Northern Morocco, a region characterized by its unique biodiversity and favorable climatic conditions [52], are combined with 150 mL of deionized water, and heated to 60 °C for approximately 30 min in order to produce the respective plant extracts. After forming, the crude extracts are filtered using Whatman No. 1 filter paper. Afterwards, 10 mL of the extract are added dropwise to 200 mL of 5 g solution of copper(II) sulphate pentahydrate ($CuSO_4.5H_2O$, Sigma-Aldrich, >99 % purity). After the extract's addition, the mixture is heated to 80 °C for two hours while being constantly stirred at 400 rpm using a magnetic stirrer. The solution's color steadily changed from blue to green, dark green, brown, and dark brown over various time intervals, signifying the reaction's completion after some intermediate stains. The solution is centrifuged for 15 min at 6000 rpm and subsequently, the NP are repeatedly cleaned with double-distilled water to get rid of any remaining biological material. Finally, black-powder CuO NPs are annealed for two hours at 800 °C in air to improve crystallinity [53]. A schematic representation of the proposed mechanism of green synthesized CuO NPs is displayed in Fig. 1.

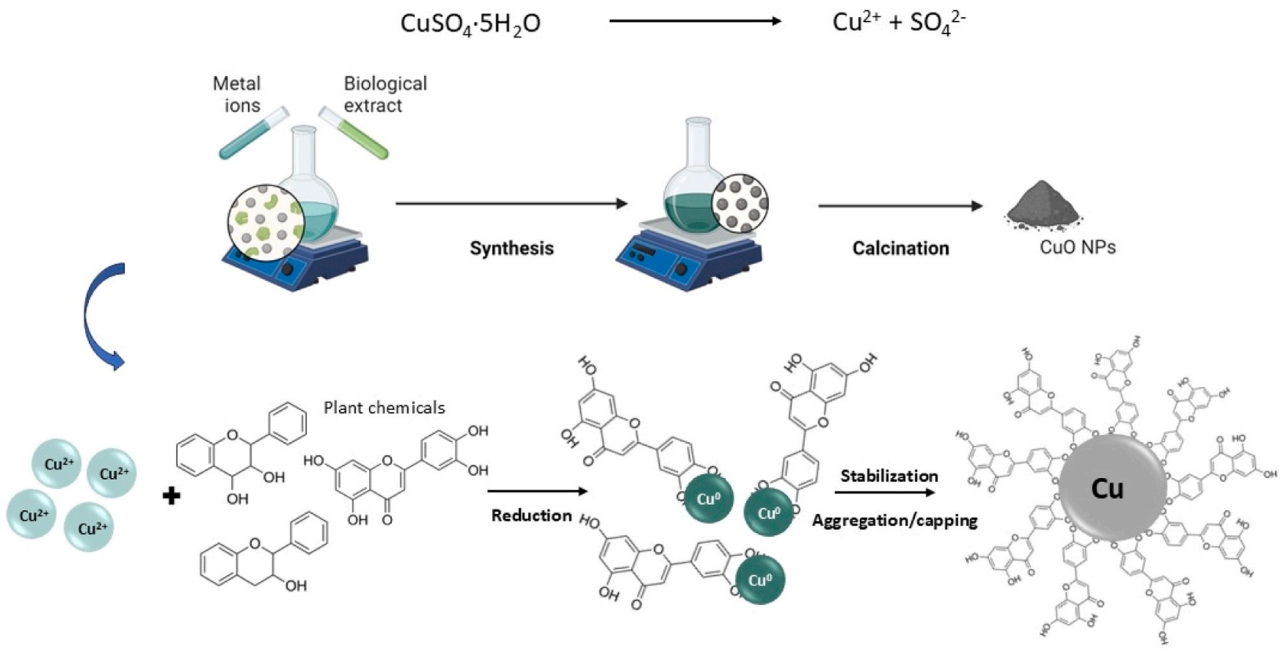

Fig. 1. Proposed mechanism of CuO NPs green synthesis via copper sulfate and plant extract interaction.

2.3. Photocathode preparation

The automated fabrication of the photocathodes is performed using an automated spray pyrolysis system (Fig. S1), specifically designed for precise control and repeatability, ensuring uniform application of the catalytic ink. Specifically, the porous Toray carbon paper support (TGP-H-60) is coated with a uniform layer of prepared catalytic ink in a gas diffusion layer (GDE) structure. This ink is composed of a blend of isopropanol (Sigma Aldrich, 99.5 %), a Nafion ® solution (Alfa Aesar, 5 % by weight, polytetrafluoroethylene copolymer), and the synthesized CuO NPs. After sonicating the resultant dispersion for at least thirty minutes, a homogenous suspension is formed and applied onto the carbon paper substrate. The optimal spray pyrolysis conditions include a nozzle height of 33 mm, a step distance of 1 mm, and an ink flow rate of 20 $mL.h^{-1}$ To ensure that all solvent had evaporated, the air brushing procedure is conducted at a temperature of 70 °C. A final loading of 1 mg cm^{-2} is achieved by continuous weighing during the continuous accumulation of layers [54].

The photocathodes tested in this study, their nomenclature, synthesis methods, and the plant extracts used are summarized in Table 1.

2.4. Material characterization

CuO NPs characterization: A QUATTRO SFEG-Thermofisher scientific scanning electron microscope coupled with Energy Dispersive X-ray spectroscopy (*SEM-EDS*) is used to observe particle size and external morphology of the particles using an accelerating voltage of 15 kV and a working distance of 10 mm. Fourier transform infrared (*FTIR*) spectrometer (PerkinElmer, Inc. Waltham, MA, USA) was used to obtain *FTIR* spectra of all samples. The crystallinity and chemical composition is assessed using an Empyrean reflection-transmission spinner diffractometer (Malvern Panalytical Ltd., Malvern, UK) with a X-ray tube equipped with an anticathode of Cu. The diffractograms are obtained by scanning over an angular range between 10.04° and 79.94° (2θ), with a step size of 0.066° and a scan step time of 113.20 s.

Photocathodes characterization: *XRD* data of the fresh and used surfaces were carried out using a PANalytical X'Pert PRO diffractometer equipped with Cu Kα radiation (λ = 1.5406 Å) at room temperature. The instrument was operated at 40 kV and 40 mA and diffraction data were collected in a 2θ range of 5° to 70° with a step size of 0.02° using a continuous scan mode. A PIXcel detector was employed. Scanning electron microscopy (*SEM*) is conducted with a JEOL JSM-7000 F field emission microscope, which features a Schottky-type electron gun, secondary electron (*SE*) detector, backscattered electron (*BSE*) detector, and Oxford's INCA X-sight Series Si (Li) penta-FET energy-dispersive X-ray spectroscopy (*EDS*) detector for spot, line, and mapping analysis. *SEM* images are acquired both on the surface and on the cross section of the selected fresh/used photocathodes at different magnifications. Both secondary electron (*SE*) and backscattered electron (*BSE*) detectors are utilized for generating images, with additional elemental mapping performed using *EDS*. The laser absorptivity of the prepared surfaces is assessed through diffuse reflectance spectroscopy (DRS). This analysis is conducted over the 220–2200 nm wavelength range using a UV-Visible-NIR JASCO 770-V spectrometer, equipped with an integrating sphere coated with Spectralon and offering a spectral resolution of 1 nm. A Spectralon reference is used for 100 % reflectance measurements, while internal attenuators are employed to establish zero reflectance and minimize background noise. For DRS measurements, photocathodes are directly placed in the holder. The reflectance spectra obtained are converted to Kubelka-Munk (K-M) units using the equation: $F(R) = (1–R\infty)^2 / (2 \cdot R\infty)$, where R∞ represents the reflectance ratio of the sample to the standard.

Table 1
CuO-based photocathodes tested and their nomenclature, synthesis method, and plant extract used.

Photocathode nomenclature	Synthesis method	Plant extract used
CuO-R	Green synthesis	Salvia rosmarinus (Rosemary)
CuO-L		Laurus nobilis (Laurel)
CuO-O		Origanum vulgare (Oregano)
CuO-P	Chemical synthesis	None

2.5. PEC cell description and experimental conditions

The continuous on-off PEC reduction of CO_2 is carried out using a modified commercial filter-press cell reactor (Electrocell, Denmark), employing the prepared CuO as the photocathode, a platinized titanium plate as the dark anode, and an Ag/AgCl (sat. KCl) reference electrode

assembled close to the cathode (Fig. S2). A Nafion 117 cation-exchange membrane is utilized as compartment separator. A 0.5 M $KHCO_3$ aqueous solution is used as catholyte and anolyte, which are pumped to the cell by two peristaltic pumps (Watson Marlow 320, Watson Marlow Pumps Group) at 30 mL·min^{-1}. A visible LED light (100 mW·cm^{-2}) is used to illuminate the photocathode (geometric area — 10 cm^2). In this study, the filter-press system possesses three inputs (catholyte, anolyte, and CO_2 separately) and two outputs (catholyte-CO_2-reduction products and anolyte), which make possible the formation of a gas–solid–liquid interface for the continuous reduction of CO_2 in the gas phase, with a CO_2 flow rate of 200 mL·min^{-1}.

For PEC characterization, each photocathode is subjected to a chronoamperometry (CP) for 30 min at a constant voltage of –1.8 V (vs. Ag/AgCl), using an AutoLab PGSTAT 302 N (Metrohm Hispania). Once the photocurrent obtained is stabilized, Linear Sweep Voltammetry (*LSV*) analyses are performed between –2.2 and –0.8 V (vs. Ag/AgCl), at a scan rate of 10 mV·s^{-1}). Additionally, sets of Cyclic Voltammetry (CV) are performed between 0 and 2 V (vs. Ag/AgCl) at a scan rate of 100 mV·s^{-1} to evaluate the electrochemical response of the different photocathodes. A potentiostat (AutoLab PGSTAT 302 N) is used to control the applied potential (E) and measure the generated current density (j) during PEC characterization tests [55].

The measured potential V versus Ag/AgCl was converted to the reversible hydrogen electrode (RHE) scale according to the Nernst equation:

$$E_{RHE} = E_{Ag/AgCl} + 0.059pH + E^{\circ}_{Ag/AgCl}$$

where ERHE is the converted potential versus RHE, $E^{\circ}_{Ag/AgCl} = 0.1976$ at 25 °C, and $E_{Ag/AgCl}$ is the experimentally measured potential against Ag/AgCl reference.

The experiments for PEC CO_2 reduction in continuous mode are performed by duplicate during 60 min at constant current density of −10 mA·cm^{-2}, both under dark and light operation. Liquid samples are taken at the reactor outlet every 15 min to measure the concentration of products obtained in each experiment. A final average concentration is calculated for each test. Values that are two times lower/higher than the average value are discarded. The production of alcohols is analyzed using a gas chromatograph (GCMSQP2010 Ultra, Shimadzu) equipped with a flame ionization detector. The production of formate is measured via ion chromatography (IC, Dionex ICS 1100).

The performance of the process is evaluated by the following indicators [55]:

– The production rate (r), which represents the formation rate for each product per unit of area and time (μmol·m^{-2} s^{-1}):

$$r = \frac{N_F}{A}$$

where N_F is described as the molar flux of the product (μmol·s^{-1}) and A is the photocathode geometric area (m^2).

– Reaction selectivity (S), which is defined as the proportion of the reaction rate for a specific product relative to the cumulative reaction rates for all products:

$$S = \frac{r_{specific\ product}}{r_{total}}$$

Where $r_{specific\ product}$ is the production rate of the target product, and r_{total} is the sum of production rates for all detected products.

– The Faradaic Efficiency (*FE*), defined as the percentage of the total charge applied to the system that is actually used to produce any target reduction:

$$FE(\%) = \frac{\varkappa \eta F}{\mathscr{C}} \times 100$$

where $\varkappa$ is the theoretical number of electrons exchanged to form the target product, η is the number of moles produced, F represents the Faraday constant (96485 C.mol^{-1}), and $\mathscr{C}$ is the total charge (C) applied in the process.

– Energy Efficiency, *EE*, which describes the amount of the total supplied energy that is employed in the conversion of CO_2 into each target product:

$$EE(\%) = FE\frac{E_T}{E_{Cathode}}$$

where E_T is the theoretical potential for CO_2 reduction to products (V), and $E_{Cathode}$ represents the cathodic potential (V).

3. Results and discussion

3.1. Characterization of synthesized CuO NPs

The *PXRD* patterns (Fig. 2.) confirm that the green synthesized copper oxide nanoparticles (CuO-R, CuO-L, and CuO-O) exhibit the monoclinic phase of CuO (tenorite, ICDD PDF No. 01–080–1268), as evidenced by the characteristic diffraction peaks at 2θ values around 32.5°, 35.5°, 38.7°, and 48.8°. These results indicate high crystallinity across the green synthesized samples. In contrast, the *PXRD* pattern of the chemically synthesized CuO-P shows additional peaks corresponding to a copper sulfate hydroxide ($Cu_3(SO_4)(OH)_4$), commonly known as antlerite (PDF No. 01–076–1621), as well as traces of sodium sulfate (Na2SO4, thenardite, PDF No. 00–001–1009), indicating the presence of impurities, formed as byproduct during the chemical synthesis process under the applied conditions. This confirm that the CuO-P sample consists of mixed phases, while CuO remains the dominant component. The absence of secondary phases in CuO-R, CuO-L, and CuO-O underscores the ability of green synthesis to produce phase-pure CuO nanostructures, highlighting a major advantage of plant-mediated approaches.

The *FTIR* spectra (Fig. 3a.) display key peaks indicative of CuO formation across all samples, with distinct differences in the eco-friendly versus chemically synthesized nanoparticles. The peaks between 400 and 600 cm^{-1} correspond to Cu–O stretching vibrations, confirming the presence of CuO in all samples [56,57]. The peak around 1050 cm^{-1}, observed in all eco-synthesized (CuO-R, CuO-L, and CuO-O) samples, may be attributed to C–O stretching vibrations of residual alcohols, phenols, or ether groups, or C–N vibrations from amine-containing compounds [58]. These residues are likely derived from the plant extracts used during synthesis and may remain partially bound to the

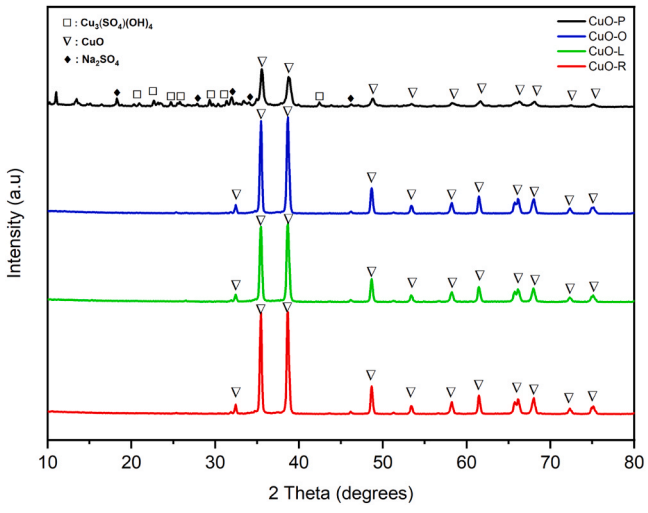

Fig. 2. *PXRD* patterns of prepared CuO-R, CuO-L, CuO-O, and CuO-P powder catalysts.

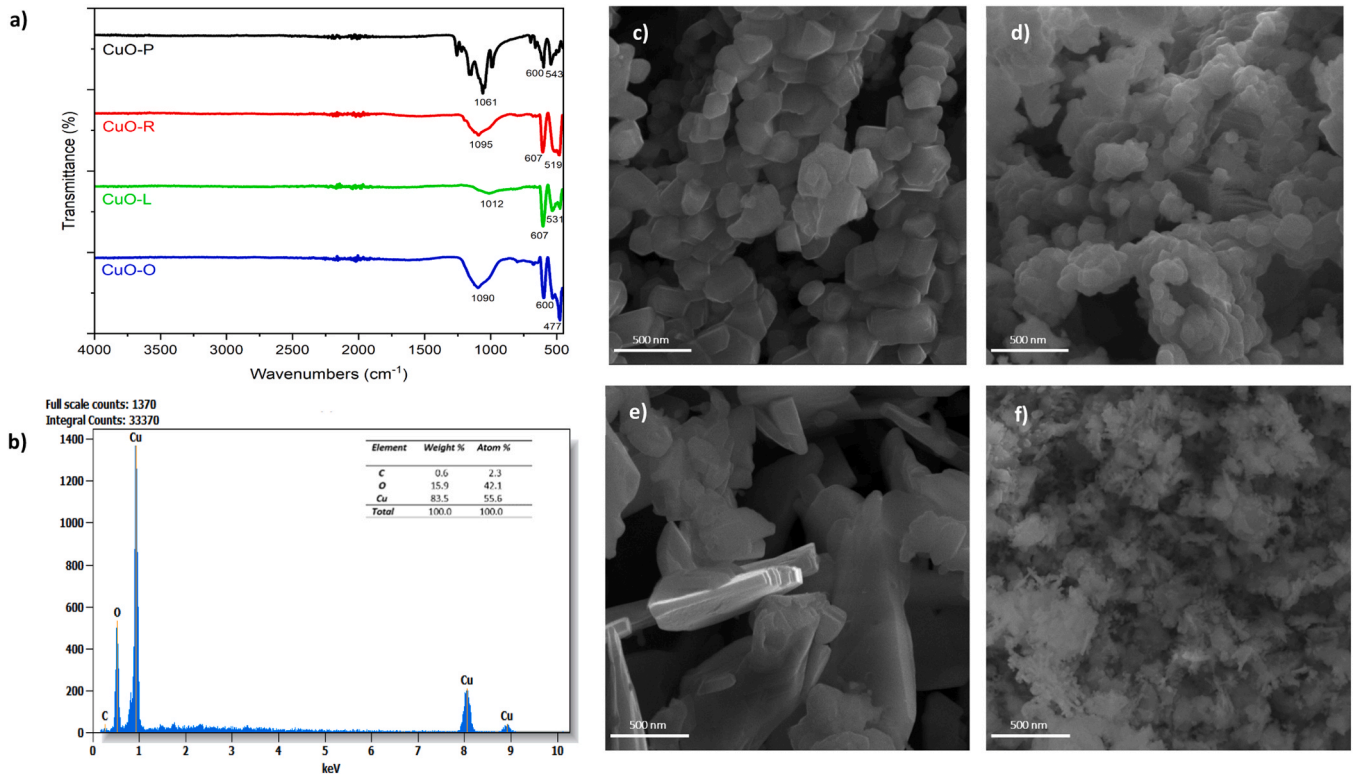

Fig. 3. Morphological and chemical characterization of CuO catalysts. (a) *FTIR* spectra of synthesized CuO NPs, (b) *EDS* mapping of CuO-R NPs, (c) – (f) *SEM* images of CuO-R, CuO-L, CuO-O, and CuO-P catalysts respectively.

nanoparticle surface, even after thermal treatment. While such organic moieties are often considered impurities, previous studies have shown that certain plant-derived compounds can act as reducing and stabilizing agents during nanoparticle formation, influencing surface chemistry and morphology [59,60]. The presence of residual phytochemicals might contribute to surface passivation or alter surface states, potentially affecting PEC performance. In the case of the chemically synthesized sample (CuO-P), the band around 1090 cm^{-1} can be ascribed to S–O stretching vibration modes originating from sulfate impurities, which are commonly observed around 1150–1000 cm^{-1} [61].

The *EDS* spectrum (Fig. 3b.) shows strong signals for Cu and oxygen (O), confirming the presence of CuO NPs. The weak carbon (C) signal observed in green-synthesized samples is consistent with *FTIR* findings and supports the presence of residual organic compounds. The chemically synthesized sample (CuO-P) displays other minor elements such as sodium (Na) and sulfur (S), (Fig. S3).

The *SEM* images (Fig. 3c-d.) reveal distinct size and morphological characteristics of CuO NPs synthesized via both green synthesis and chemical methods. CuO-R particles, averaging 139 nm, exhibit a relatively uniform and well-defined shape, suggesting controlled formation, possibly stabilized by phytochemicals like rosmarinic acid from *Salvia rosmarinus* [62]. CuO-L (*Laurus nobilis*), with an average size of 80 nm, appears in denser clusters, indicating a more compact morphology that could increase surface area [63]. CuO-O particles (~115 nm), synthesized with *Origanum vulgare*, display an irregular, rod-like morphology, likely due to the influence of phytochemicals such as thymol and carvacrol, which may promote anisotropic growth. Such a structure might enhance light absorption but potentially reduce the stability [64]. In contrast, the chemically synthesized CuO-P, with an average size of 37 nm, shows smaller and highly uniform particles. This difference can be attributed to the absence of specific phytochemicals present in plant extracts, which influence particle growth and aggregation [65,66]. As a result, the chemical synthesis method produces more homogeneous and finer particles compared to the eco-friendly methods.

These morphological differences align with the *HPLC* results obtained from aqueous extracts (Tables S2-S4), which revealed distinct phytochemical profile for each plant. *S. rosmarinus* contained high levels of rosmarinic acid and luteolin, both known to facilitate nucleation and stabilize particle dispersion [67]. *O. vulgare* extract is rich in caffeic acid, and flavonoid aglycones, which promotes directional growth and surface heterogeneity [68]. In *L. nobilis*, catechins and rutin may have contributed to particle condensation and surface compaction [69]. This correlation between phytochemical composition and nanoparticle morphology supports the critical role of plant-derived polyphenols in modulating green nanoparticle synthesis.

The green synthesis led to well-defined CuO nanostructures with distinct morphological and surface characteristics. The CuO-R, CuO-L, and CuO-O samples exhibited larger particle sizes compared to the chemically synthesized CuO-P, likely due to the presence of residual phytochemicals acting as natural capping agents. The annealing step at 800°C in air ensured the complete transformation of precursor phases into well-crystallized CuO and the removal of most organic residues from plant extracts. However, minor traces of plant-derived mineral impurities (such as aluminosilicates or calcium sulfate) are still detected on the electrode surface. The residual presence of phytochemical-derived organic compounds, even after calcination, may also contribute to the surface passivation and influence the optical absorption properties, potentially enhancing charge separation during PEC operation [70,71]. Such differences in nanoparticle distribution and surface morphology are known to influence the availability of active sites. As reported in literature, nanoscale structuring and surface texture can significantly impact CO_2 adsorption and product selectivity in photocatalytic systems [72,73]. These observations support the proposed biosynthesis mechanism (Fig. 1.), in which plant-derived flavonoids and polyphenols act transient reducing and stabilizing agents during the nucleation and growth of CuO nanoparticles. While most organic moieties decompose during 800°C annealing step [74,75], the weak *FTIR* band around 1050 cm^{-1} and minor carbon signal in *EDS*

spectra are consistent with trace residuals. This indicates that plant molecules primarily influence nanoparticle formation during early synthesis stages, rather than remaining as stable surface-bound ligands.

3.2. Surface characterization of fresh GDEs

The X-ray diffraction (*XRD*) analysis of the four electrodes confirmed the presence of the tenorite phase of CuO (ICDD PDF No. 01–080–1268, space group C2/c) in all samples, demonstrating its successful integration into the GDEs, as can be seen in Fig. 4. In the chemically synthesized CuO electrode (CuO-P-F), the CuO reflections are detected with relatively low intensity, exhibiting only its two main peaks (at 2θ values of 35.6 and 38.8°). Additionally, traces of copper sulfate hydroxide ($Cu_3(SO_4)(OH)_4$, Antlerite, PDF No. 01–076–1621) and sodium sulfate (Na_2SO_4, Thenardite, PDF No. 00–001–1009) are identified as byproducts of the chemical synthesis process. In contrast, the plant leaf-derived CuO electrodes (CuO-R-F, CuO-L-F, and CuO-O-F) displayed more pronounced CuO reflections, with multiple peaks visible, indicating a higher amount of CuO present. As expected, in all GDEs the characteristic peaks of graphite at 2θ values of 26.6 and 54.6° (PDF No. 00–008–0415) and PTFE (polytetrafluoroethylene polymer, PDF No. 00–047–2217) from the carbon paper support are observed in all cases. All the identification are made on the basis of the data retrieved from the Powder Diffraction [76].

Scanning Electron Microscopy (*SEM*) analysis of the fresh (CuO-X-F) and used (CuO-X-U) surfaces is conducted at various magnifications using secondary electron (SE) and backscattered electron (BSE) detectors coupled with energy-dispersive X-ray spectroscopy (*EDS*) for the generation of the images (Fig. S5–S24).

As a representative example of GDEs prepared from plant leaf-derived CuO, Fig. 5a. displays SE images at 1kX magnification of the CuO-L-F electrode surface, along with a *BSE* image and *EDS* mapping of a selected area. The surface appears mainly covered by CuO particles exhibiting broad size polydispersion, from nanometric sized particles (50–100 nm) to micrometric ones (1–3 μm). This size range is broadly consistent with the particle sizes observed in the corresponding CuO powders (Fig. 3.), confirming that the initial particle dimensions are largely preserved after electrode fabrication, although localized clustering is visible on the GDE surface, particularly in CuO-L and CuO-O. Interestingly the *EDS* mapping of the surface revealed a minor presence of aluminosilicates (depicted as orange spots) ascribable to the soil particles present in the employed dried leaf powder. Further details can

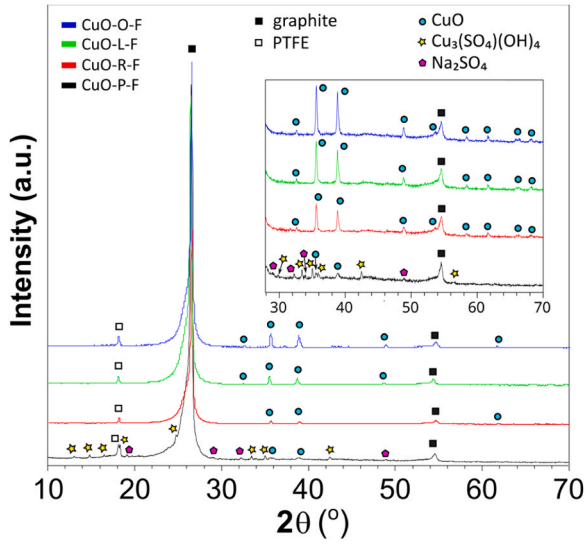

Fig. 4. *PXRD* diffraction patterns of fresh CuO-P, CuO-R, CuO-L and CuO-O–based prepared GDEs.

be found in Fig. S7-S9. Similar features are found for CuO-O-F and CuO-R-F electrodes (Fig. S10-S15), in which apart from aluminosilicate particles, few calcium sulfate crystallites are observed dispersed in the matrix of copper(II) oxide. It is important to note that calcium sulfate is likely formed during the synthesis process due to the combined presence of calcium (traces found in the pristine leaves) and sulfate ions (originating from the copper(II) sulfate reagent). The low solubility of this compound hinders its complete removal during the washing step of the synthesis product.

On the other hand, in CuO-P-F sample (Fig. 5b) CuO appears mainly as micrometric crystallites (green colored), accompanied by a significant amount of sodium sulfate hexagonal crystallites (purple colored) formed as a by-product of the chemical synthesis.

Fig. 6. shows the UV-Vis-NIR absorption spectra of the four freshly prepared photocathodes. All samples exhibit significant absorption in the visible spectrum, confirming their potential for PEC applications under visible-light irradiation [77]. Among them, CuO-O-F, CuO-R-F and CuO-L-F show similar absorption profiles with an absorption onset around 800 nm, consistent with CuO's typical bandgap (~1.2–1.7 eV). This suggests similar crystallinity and electronic properties for the surfaces prepared from CuO NPs obtained by plant extract [78]. CuO-P, in contrast, displays a distinct absorption profile, with two apparent absorption edges in the visible region (~600 nm and ~800 nm), likely due to the presence of other components apart from the CuO NPs ($Cu_3(OH)(SO_4)$ and Na_2SO_4 phases). Additionally, CuO-R-F's lower annealing temperature and so smaller particle size and more uniform nanoparticle dispersion, as seen in *SEM*, may contribute to this modified light-harvesting properties, which could influence its PEC performance differently than the pure CuO electrodes. The *SEM* analysis (Fig. 5) further supports these trends, showing variations in particle distribution and morphology that can impact charge transport and recombination rates [79].

Band gap values were not extracted from these spectra, as the presence of the carbon substrate and additional components limits the reliability of Tauc analysis under these conditions [80,81]. However, the intrinsic bandgap of monoclinic CuO is well established in the literature, typically ranging between 1.2 and 1.7 eV.

3.3. PEC characterization

Fig. 7. displays the on-off performance of green synthesized CuO-based photocathodes through chronoamperometry (CP), linear sweep voltammetry (LSV), and cyclic voltammetry (CV) analyses. These techniques were employed under fixed or sweeping voltage conditions to evaluate photocurrent response and photoactivation behaviour, whereas product formation and Faradaic efficiencies were assessed separately under galvanostatic operation at a constant current density of $-10\ mA{\cdot}cm^{-2}$.

The CP data (Fig. 7a.) demonstrates the time-dependent current density (j) response of the photocathodes under both illuminated and dark conditions at a constant voltage of −1.18 V vs. RHE. As anticipated, all photocathodes exhibit increased current densities when exposed to light. Among them, CuO-R exhibits the highest photocurrent ($\sim$-1.6 $mA{\cdot}cm^{-2}$). This stable photocurrent response under constant illumination supports the short-term operational stability of the photocathodes. Such behaviour aligns with recent reports where phytochemical-derived surface layers protected metal oxide nanostructures under electrochemical stress by passivating defects and preventing aggregation [82]. Similar evidence also shows that plant metabolites can serve as effective capping and stabilizing agents during green synthesis [83].

The substantial photocurrent of CuO-R can be directly attributed to its favourable surface morphology and enhanced surface properties, as evidenced by the combined powder and electrode characterizations (Figs. 3 and 5). As shown in the powder characterization results (Fig. 3.), CuO-R consists of relatively uniform, well-defined particles, stabilized

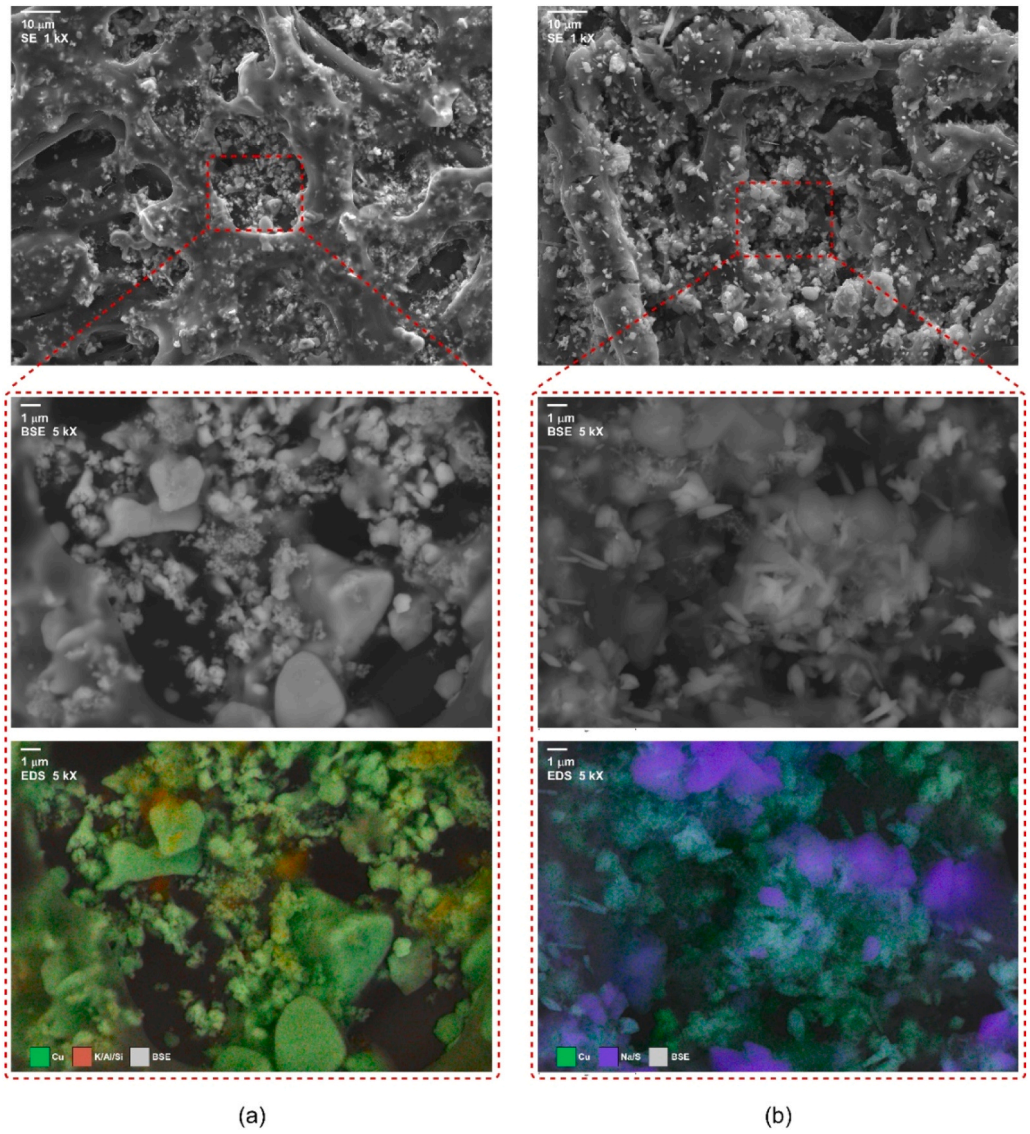

Fig. 5. SEM images at 1 KX magnification (up), showing for the highlighted area BSE images (middle) and EDS mapping (down) at 5 kX magnification of (a) CuO-L-F and (b) CuO-P-F electrode surfaces.

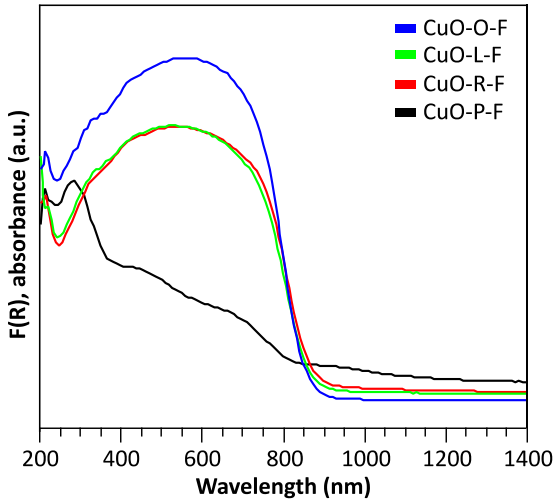

Fig. 6. UV-Vis-NIR absorption spectra derived from Kubelka-Munk function for prepared fresh surfaces.

by rosmarinic acid and other phytochemicals present in *Salvia rosmarinus* [84]. These phytochemicals act as natural reducing agents during CuO formation, while simultaneously serving as capping agents, which for CuO-R, effectively prevented excessive particle aggregation and ensured the formation of well-dispersed nanoparticles with enhanced crystallinity [85–87]. This observation is consistent with the surface characterization of the CuO-R-F electrode, where a relatively homogeneous particle distribution with broad size polydispersity is observed, confirming good dispersion during the spray pyrolysis process. The phytochemical-derived surface stabilization observed in CuO-R contrasts with the denser particle clusters seen in CuO-L and the irregular rod-like particles in CuO-O. For CuO-L, the more compact morphology may lead to poorer charge separation, as the proximity of nanoparticles may prevent effective electron transport across the photocathode [88, 89]. In CuO-O, the anisotropic, rod-like morphology, influenced by thymol and carvacrol from *Origanum vulgare*, may enhance light scattering, but at the cost of lower structural uniformity and reduced surface stability [90]. These morphological differences directly affect the surface charge transfer properties, ultimately impacting photocurrent generation of these electrodes during PEC operation.

In contrast, the chemically synthesized CuO-P, with its smaller and

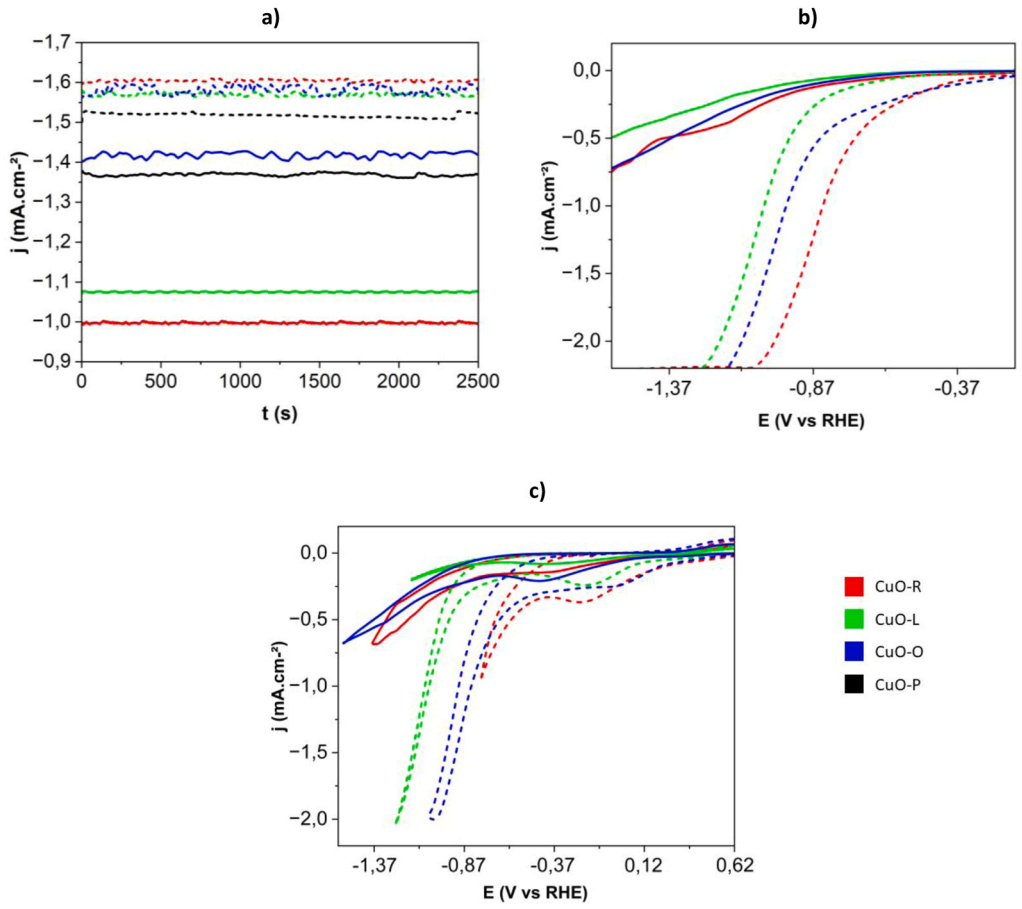

Fig. 7. PEC characterization of CuO-based photocathodes in dark (continuous line) and under visible illumination (dotted line; 100 mW·cm^{-2}), (a) *CP* at −1.18 V vs RHE, (b) *LSV*, (c) *CV*.

more uniform particles, benefits from a highly homogeneous surface (Fig. 3.), which contributes to decent photocurrent performance. However, the absence of phytochemical stabilizers and the use of different reagents during their synthesis leaves CuO-P NPs more susceptible to impurity incorporation, as evidenced by the presence of sodium sulfate crystallites in the CuO-P-F surface (Fig. 5b.) [91,92]. These residual impurities, originating from the chemical synthesis process, could introduce localized defects that partially hinder charge transport compared to the phytochemical-coated CuO-R.

The *LSV* curves (Fig. 7b.) further highlight these performance differences, with CuO-R exhibiting both the most positive onset potential and the highest photocurrent density under illumination. This superior behaviour confirms the synergistic role of phytochemical-induced surface properties, improved crystallinity, and enhanced light absorption, all of which contribute to improved charge separation and PEC CO_2 reduction efficiency [93,94]. To make the distinction between characterization and operational conditions, the onset potentials presented in Fig. 7b. were obtained under voltage-sweeping mode and serve the photocurrent response and light activation behaviour of the photocathodes. In contrast, product formation and *FE* were evaluated under galvanostatic conditions, applying a fixed current density of −10 mA·cm^{-2}, during which the operating potentials stabilized around −0.37 V vs RHE (Table 2 and Fig. 8.). Therefore, product selectivity reflects continuous PEC operation at constant current rather than the *LSV* curves.

The *CV* data (Fig. 7c) further confirms the trends observed in *CP* and *LSV*. Under dark conditions, CuO-R, CuO-L, and CuO-O exhibit minimal catalytic activity, as evidenced by the low current densities reached. However, upon illumination, significant increases in current density are observed for all electrodes, with CuO-R demonstrating the highest photoactivity. This reflects superior charge transfer dynamics and enhanced photoelectrocatalytic activity, further confirming CuO-R as

Table 2
r and *EE* with and without illumination (j = -10 mA·cm^{-2}).

CuO-NPs		*E (V vs RHE)*	*r (μmol·m^{-2}·s^{-1})*			*EE (%)*		
			HCOO$^-$	*CH_3OH*	*C_2H_5OH*	*HCOO$^-$*	*CH_3OH*	*C_2H_5OH*
CuO-R	*Dark*	*−0.99*	*70.9 ± 4.8*	*211.9 ± 12.5*	*21.2 ± 2.2*	*3.3*	*27.8*	*4.9*
	Light	*−0.37*	-	*272.6 ± 15.1*	*69.8 ± 3.7*	-	*39.2*	*18.1*
CuO-L	*Dark*	*−0.95*	*36.1 ± 1.9*	*161.1 ± 10*	*36.0 ± 2.3*	*1.9*	*24.6*	*9.8*
	Light	*−0.46*	-	-	*31.8 ± 3*	-	-	*17.9*
CuO-O	*Dark*	*−0.96*	-	-	*49.1 ± 2.8*	-	-	*8.2*
	Light	*−0.80*	-	-	*74.8 ± 3.7*	-	-	*13.9*
CuO-P	*Dark*	*−0.90*	*43.4 ± 3*	-	*82.1 ± 5.8*	*3.3*	-	*31.9*
	Light	*−0.75*	*50.6 ± 3.3*	-	*1113.9 ± 86*	*0.3*	-	*38.2*

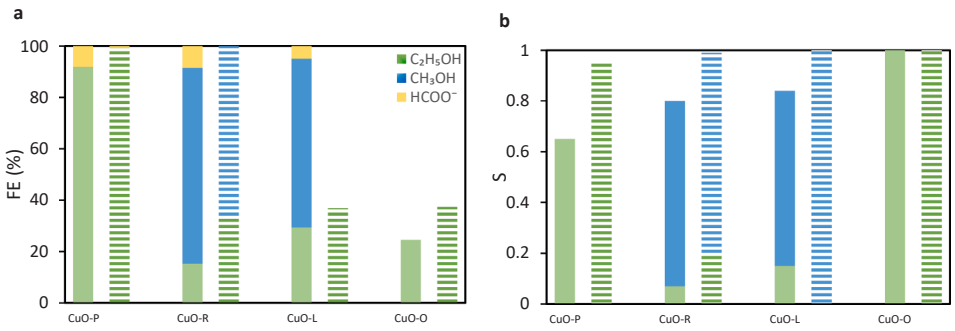

Fig. 8. (a) *FE* of CO_2 reduction products for CuO-based photocathodes under dark (solid fill) and light (patterned fill) conditions, (b) reaction selectivity for alcohols under the same conditions.

the most effective photocathode in this study.

Overall, the superior PEC performance of CuO-R can be directly attributed to its favourable surface morphology, phytochemical-induced stability, and enhanced photoactivity, as demonstrated by the combined analysis of powder, electrode, and after-use characterization data. In addition, the limited presence of residual phytochemicals, as shown by FTIR and EDS, may contribute to surface passivation by mitigating trap states and thus support more efficient charge separation during PEC operation, as proposed in previous studies [95,96]. This passivation effect likely reduces recombination losses at the CuO surface and enhances interfacial charge transfer. The higher photocurrent densities and more positive onset potential observed for CuO-R (Fig. 7b.) are consistent with improved charge separation and transport efficiency. These results suggest that the phytochemical residues from the plant extract play a beneficial role in tuning the semiconductor–electrolyte interface. The comparison between CuO-R and CuO-P underscores the advantages of green synthesis methods, while the weaker performance of CuO-L and CuO-O highlights the critical influence of the specific phytochemical profile of each plant extract on the final PEC performance [97].

3.4. Product distribution and system efficiency

Fig. 8a. presents the *FE* of the different measured CO_2 reduction products (ethanol, methanol, and formate) as a function of the tested CuO-based photocathodes CuO-P, CuO-R, CuO-L, and CuO-O under both dark and light conditions at galvanostatic conditions (-10 $mA{\cdot}cm^{-2}$), while Fig. 8b. highlights the reaction selectivity (S) toward alcohols (ethanol and methanol) under the same conditions.

Moreover, Table 2 summarize the required external potentials to achieve the fixed current density, *r*, and *EE* for the tested photocathodes under both illumination and dark conditions.

The CuO-R photocathode, prepared with *Salvia rosmarinus* extract, demonstrates a substantial reduction in applied potential from −0.99 V in the dark to −0.37 V (vs. RHE) under illumination. In the dark, methanol is the primary product with an *FE* of 76.2 % and a reaction rate of 211.9 $\mu mol{\cdot}m^{-2}{\cdot}s^{-1}$, which is accompanied by formate production at 8.5 % (70.9 $\mu mol{\cdot}m^{-2}{\cdot}s^{-1}$) and ethanol at 15.3 % (21.2 $\mu mol{\cdot}m^{-2}{\cdot}s^{-1}$). Under visible light, methanol remains the dominant product with an *FE* of 66.1 % and a reaction rate of 272.6 $\mu mol{\cdot}m^{-2}{\cdot}s^{-1}$, while ethanol reaches 33.8 % (69.8 $\mu mol{\cdot}m^{-2}{\cdot}s^{-1}$) and formate is no longer detected. These findings are consistent with the reaction selectivity for CuO-R (Fig. 8b) and the performance metrics summarized in Table 2, where methanol is the main reduction product, shifting from 73 % in the dark to 79 % under light, and ethanol selectivity increases from 7 % to 20 %. The enhanced selectivity and higher reaction rates of CuO-R can be directly linked to its well-preserved surface morphology and the phytochemical-induced stabilization observed in the fresh electrode. The *EE* improves from 27.8 % in the dark to 39.2 % under illumination for methanol. Comparatively, studies in CuO/g-C_3N_4 photocathodes demonstrate a *FE* of 75 % for methanol production with enhanced performance, even though CuO-R shows superior *EE* with lower external potentials needed [98,99].

The CuO-L photocathode, synthesized with *Laurus nobilis* extract, demonstrates a reduction in applied potential from −0.95 V in the dark to −0.46 V (vs. RHE), indicating improved *EE* under light conditions. In dark conditions, methanol is the primary product with a *FE* of 65.7 % and a reaction rate of 161.1 $\mu mol{\cdot}m^{-2}{\cdot}s^{-1}$, while ethanol presents a *FE* of 29.4 % (36.0 $\mu mol{\cdot}m^{-2}{\cdot}s^{-1}$) and formate displays a value of 4.9 % (36.1 $\mu mol{\cdot}m^{-2}{\cdot}s^{-1}$). Under light, ethanol becomes the sole product with a *FE* of 36.9 % and a reaction rate of 31.8 $\mu mol{\cdot}m^{-2}{\cdot}s^{-1}$. This shift in selectivity and relatively moderate photocurrent response under illumination are consistent with the denser particle clustering and partial agglomeration observed in CuO-L electrodes. These structural features may limit the number of accessible active sites, contributing to CuO-L's lower CO_2 reduction efficiency compared to CuO-R. The *EE* improves to 24.6 %. The moderate change in selectivity under illumination suggests a weaker photo-response in CuO-L, possibly due to less effective phytochemicals in *Laurus nobilis*. Studies involving Cu_2O-SnOx hybrids report higher formate production efficiency (*FE* ~83.3 %) at similar potentials, suggesting that while CuO-L provides a sustainable synthesis route, it may require optimization for enhanced CO_2 reduction performance [100].

The CuO-O photocathode, synthesized using *Origanum vulgare* extract, exhibits the lowest performance. The required potential decreased slightly from −0.96 V in the dark to −0.80 V (vs. RHE) under illumination, showing limited improvement in energy efficiency. In dark conditions, ethanol is the primary product, with a *FE* of 24.6 % and a reaction rate of 49.1 $\mu mol{\cdot}m^{-2}{\cdot}s^{-1}$, while methanol and formate are not detected. Under light conditions, ethanol production increases marginally to 37.4 % with a reaction rate of 74.8 $\mu mol{\cdot}m^{-2}{\cdot}s^{-1}$, while methanol and formate remain undetected. The limited photocatalytic response and poor selectivity shift correlate with the irregular morphology and suboptimal surface uniformity observed in the CuO-O-F electrode. The relatively low total *FE* observed for CuO-O can be explained by the predominance of side reactions, particularly the hydrogen evolution reaction (*HER*), which can compete with CO_2 reduction under PEC conditions. In addition, energy losses due to charge recombination, inefficient charge separation, or overpotentials within the PEC system may also reduce the effective electron utilization for product formation, as previously reported in similar PEC systems [30,100,101]. In our previous work on Cu-based electrocatalysts [17], we also observed that H_2 was a major competing product, with a *FE* of 91.1 % for C_2H_4 and significant H_2 generation (239.7 $\mu mol{\cdot}m^{-2}{\cdot}s^{-1}$ at −2.5 V vs Ag/AgCl), further confirming the of HER in reducing the total *FE* of carbon based products. These structural characteristics may limit charge transfer efficiency and reduce the availability of active sites, contributing to CuO-O's poor PEC performance. Accordingly, the *EE* values are lower than those reached for previous CuO-R and CuO-L photocathodes (8.2 % in the dark and 13.9 % under illumination), indicating possible energy

losses, likely due to suboptimal nanoparticle morphology and catalytic activity resulting from this green synthesis process [102,103].

The results for the chemically synthesized CuO-P photocathode show a contrast. Under illuminated conditions, the external bias required for CuO-P photocathode to carry out the CO_2 reduction decreases from −0.90 V in the dark to −0.75 V (vs. RHE), resulting in an increase in *EE*. In dark conditions, ethanol is the dominant product with a *FE* of 91.9 % and a reaction rate of 82.1 $\mu mol \cdot m^{-2} \cdot s^{-1}$, while formate is present at 8.1 % and methanol was not detected. Under light conditions, ethanol production exhibited nearly 100 % *FE*, while formate is reduced to 0.7 % and methanol remains undetected. The selectivity similarly shifts, with ethanol increasing from 65 % in the dark to 96 % ethanol under light. The *EE* increases from 31.9 % in the dark to 38.2 % under illumination, where this selectivity appears driven primarily by the electrocatalytic nature of CuO-P, where its well-defined surface morphology and active catalytic sites facilitate CO_2 reduction, showing minimal dependence on photoinduced mechanisms [104,105]. This behaviour may also be linked to the presence of Cu^+ species on the CuO-P surface, as the lower annealing temperature (450°C) might preserve a mixed Cu^+/Cu^{2+} oxidation state. Cu+ sites have been reported to enhance C-C coupling and ethanol production, as they can act as active centers promoting carbon chain growth during CO_2 reduction, thereby increasing selectivity toward ethanol over other product. while the fully oxidized Cu^{2+} surfaces typically lead to methanol or formate production [106,107].

The *FE* and *EE* values (Table 2) highlight the superior performance of CuO-R compared to other CuO- and Cu_2O-based photocathodes reported in the literature (Table 3). For methanol production, CuO-R achieves over 60 % *FE* under visible light irradiation at an applied potential of –1.18 V vs. RHE, which is among the highest reported. This compares favourably with other systems such as CuO/g-C_3N_4 (+0.096 V vs. RHE, 75 % *FE* for methanol [99]) and $CuFe_2O_4$/PANI (–0.004 V vs. RHE, 73 % *FE* [103]), especially considering the relatively lower external potential required in our case. Furthermore, unlike Cu_2O/PANI (–0.85 V vs. RHE, 57.6 % *FE* [102]) or CuO with MOF coatings (–1.22 V vs. RHE [98]), CuO-R enables alcohol formation at significantly reduced overpotentials. These comparisons suggest that the green synthesis route using *Salvia rosmarinus* not only enhances selectivity toward alcohols, but also improves energy efficiency. This improvement may be attributed to beneficial surface properties, enhanced light harvesting, and photoinduced charge separation inherent to the biogenic synthesis process [108].

3.5. Post-reaction characterization of used photocathodes

During the electrochemical reaction some impurities are either completely or partially removed, especially in the case of CuO-P-U, in which no traces of sodium sulfate are detected after the reaction. This suggests that the initial chemical synthesis process introduced byproducts that are washed away during PEC operation, potentially altering the photoelectrode surface. However, some of the CuO phase was retained on the photocathode surface, ensuring continued catalytic activity (Figs. 9–11. and Fig. S19-20).

Note that the *EDS* mappings and *PXRD* performed in used electrodes (Figs. 10–11 and Fig. S21-24) reveal also the presence of crystallized electrolyte ($KHCO_3$) formed after extracting the GDEs from the reaction cell. Further evidence can be found in the relative elemental contents determined by *EDS* analysis for fresh and used electrodes (Table S1).

As mentioned, the *PXRD* analysis of the used electrodes (Fig. 11) confirms that the CuO phase remains present in all cases. However, its reflection intensities are significantly reduced, suggesting potential leaching of the catalytic layer during the reaction. In the chemically synthesized electrode (CuO-P-U), the previously observed byproducts, Antlerite ($Cu_3(SO_4)(OH)_4$) and sodium sulfate (Na_2SO_4), are no longer detected, indicating their loss during the electrochemical process. Additionally, apart from the characteristic reflections of graphite and PTFE coming from the carbon paper support, reflections from potassium bicarbonate ($KHCO_3$, Kalicinite PDF No. 00–012–0292) became observable, which comes from the electrolyte used in the PEC reaction.

4. Conclusions

CuO NPs are green synthesized using *Salvia rosmarinus*, *Laurus nobilis*, and *Origanum vulgare* plant extracts, and their effectiveness as photocathodes for the PEC reduction of CO_2 is evaluated. The CuO-R photocathode, derived from *Salvia rosmarinus*, exhibited the highest performance, achieving the best faradaic efficiency (66.1 % *FE*) and production rate (272.6 $\mu mol \cdot m^{-2} \cdot s^{-1}$) for methanol under visible light, while requiring the lowest applied potential (-0.37 V vs RHE). This enhanced performance is directly linked to the favourable surface properties and enhanced structural stability provided by the phytochemicals present in the plant extract, which facilitated efficient charge separation, preserved the electrode morphology after continuous operation, and optimized CO_2 reduction selectivity towards methanol.

In contrast, CuO-L and CuO-O photocathodes, synthesized using *Laurus nobilis* and *Origanum vulgare*, respectively, showed lower photoelectrochemical performance, with CuO-L showing a shift towards ethanol selectivity under illumination and CuO-O maintaining 100 % ethanol selectivity in both dark and light conditions. The moderate activity and structural changes observed in these electrodes highlight the critical influence of the specific phytochemical profile on nanoparticle growth, surface morphology, and long-term stability. This emphasizes the importance of carefully selecting plant sources and understanding their chemical composition to optimize the properties of green synthesized photocathodes. Comparatively, the chemically synthesized CuO-P photocathode exhibits a strong electrocatalytic preference for ethanol production, reaching a *FE* of 99 % under illumination, while maintaining high structural stability. The distinction between eco-synthesized photocathodes, which some favoured methanol, and CuO-P, which strongly favoured ethanol, highlights the impact of synthesis routes on product selectivity and PEC catalytic mechanisms.

Overall, these findings demonstrate that phytochemical-assisted synthesis offers a sustainable and efficient route for developing high-

Table 3
Comparative performance of CuO-based photocathodes in PEC CO_2 reduction.

Photocathode	Anode	Potential (V vs. RHE)	Light source	Reaction medium	FE (%)	Reference
CuO-P	Pt	–1.18	Visible Light (100 mW/cm^2)	0.5 M $KHCO_3$	C_2H_5OH: 99.25 %	This work
CuO-R	Pt	–1.18	Visible Light (100 mW/cm^2)	0.5 M $KHCO_3$	CH_3OH: > 60 % C_2H_5OH: 30 %	This work
CuO/CeO_2	Pt	−1.10	-	0.1 M KHCO3	C_2H_4: 50 %	[104]
CuO	Pt/C	+ 0.096	Visible Light	0.1 M $NaHCO_3$	CH_3OH: 47 %	[99]
CuO/g-C_3N_4	Pt/C	+ 0.096	Visible Light	0.1 M NaHCO3	CH_3OH: 75 %	[99]
CuO with MOF coating	Pt	−1.22	AM 1.5 G illumination	0.1 M TBAPF6 in acetonitrile	CO: 95 %	[98]
CuO/Cu_2O	Pt	+ 0.31	AM 1.5 illumination (70 mW/cm^2)	0.1 M Na_2SO_4	CH_3OH: 95 %	[109]
Cu_2O	Pt	+ 0.34	AM 1.5 illumination (100 mW/cm^2)	0.5 M $KHCO_3$	$HCOO^-$: 38.5 %	[110]
Cu_2O/PANI	Pt	−0.85	Visible Light	0.1 M $KHCO_3$	CH_3OH: 57.66 %	[102]
Cu/p-NiO	Pt	−0.7	Visible Light	50 mM K_2CO_3	Low selectivity of $HCOO^-$	[108]
$CuFe_2O_4$/PANI	Pt	−0.004	Visible Light	0.1 M $NaHCO_3$	CH_3OH: 73 %	[103]

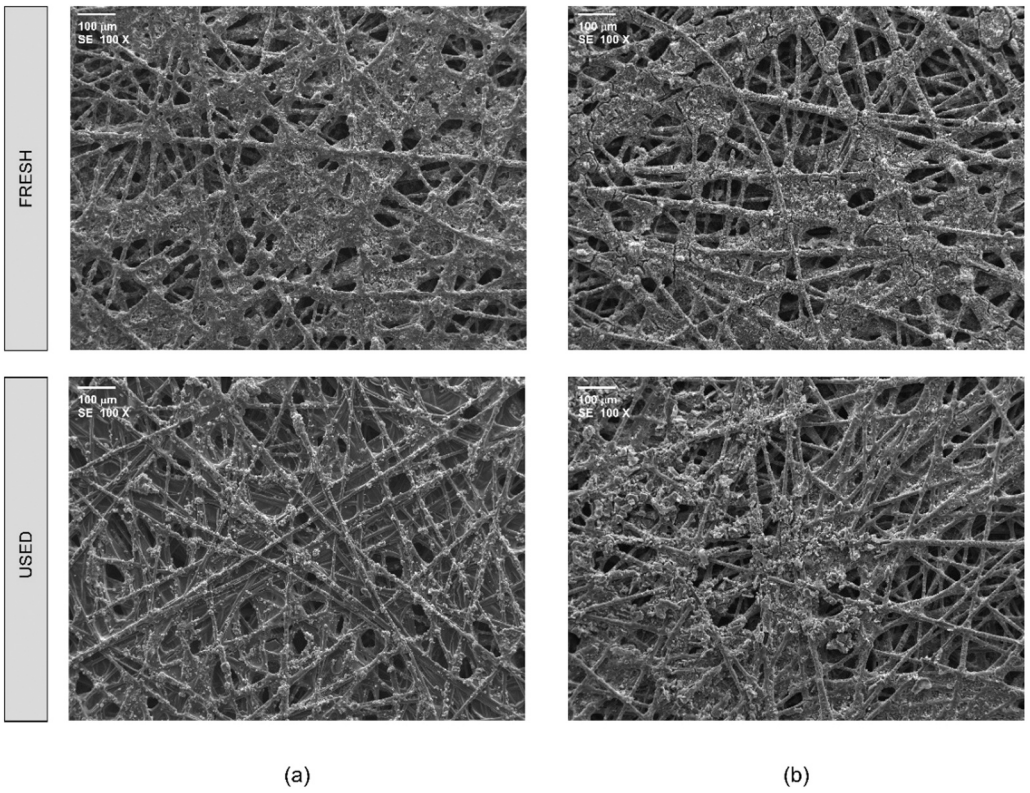

Fig. 9. *SE SEM* images at 100 X magnification for (a) CuO-L and (b) CuO-P electrodes prior and after 2 h of reaction.

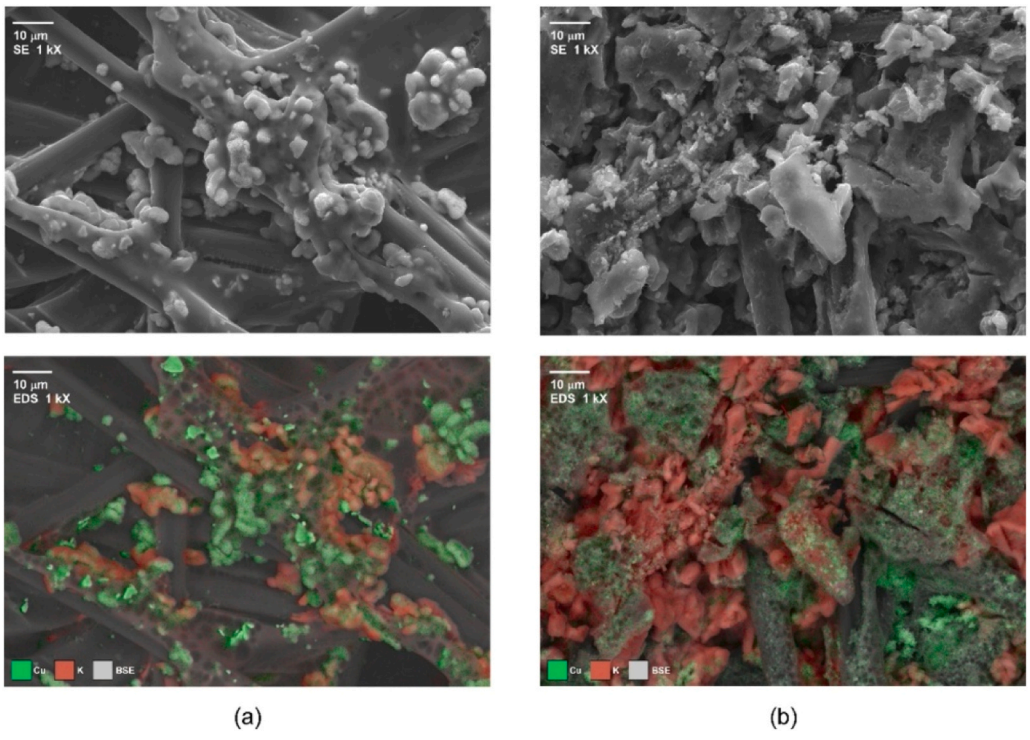

Fig. 10. *SE* (up) end *EDS* mapping (down) *SEM* images at 1 kX magnifications for surfaces of the (a) CuO-L-U and (b) CuO-P-U electrodes after 2 h of reaction.

performance photocathodes for PEC CO_2 reduction. Future work should focus on exploring a wider variety of plant extracts, correlating specific phytochemical components to nanoparticle properties, and fine-tuning deposition techniques to further improve performance and durability. Such advances could enable the scalable development of eco-friendly materials for solar-driven carbon conversion technologies.

CRediT authorship contribution statement

Amena Mrabet: Writing – review & editing, Writing – original draft,

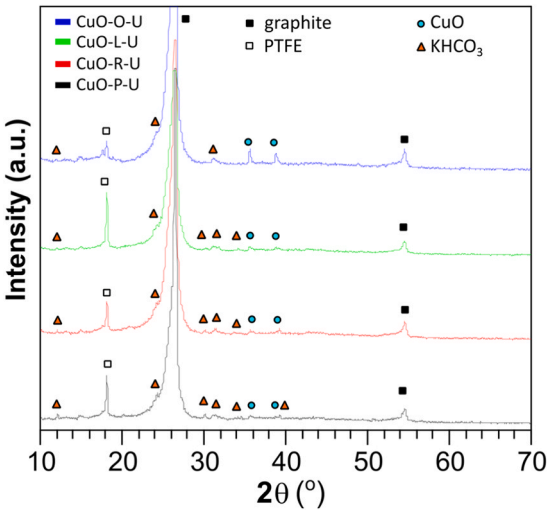

Fig. 11. *PXRD* diffraction patterns of used CuO-P, CuO-R, CuO-L and CuO-O –based GDEs after 2 h of reaction.

Visualization, Methodology, Investigation, Conceptualization. **Maite Perfecto-Irigaray:** Writing – original draft, Validation, Methodology, Investigation, Formal analysis. **Ivan Merino-Garcia:** Writing – review & editing, Writing – original draft, Visualization, Validation, Supervision, Methodology, Investigation, Conceptualization. **Mohamed Khaddor:** Writing – review & editing, Visualization, Validation, Supervision. **Garikoitz Beobide:** Writing – original draft, Validation, Methodology, Investigation, Formal analysis. **Jonathan Albo:** Writing – review & editing, Writing – original draft, Visualization, Validation, Supervision, Resources, Project administration, Methodology, Investigation, Funding acquisition, Conceptualization.

Declaration of Competing Interest

The authors declare that they have no known competing financial interests or personal relationships that could have appeared to influence the work reported in this paper.

Acknowledgments

The authors gratefully acknowledge Grant PID2022–138491OB-C31 funded by MICIU/AEI/10.13039/ 501100011033 and by ERDF, EU. Ivan Merino-Garcia also acknowledges Grant RYC2023–043378-I funded by MICIU/AEI/10.13039/ 501100011033 and by ESF +.

Appendix A. Supporting information

Supplementary data associated with this article can be found in the online version at doi:10.1016/j.jcou.2025.103222.

Data availability

Data will be made available on request.

References

[1] M. Kabir, U. Habiba, M.Z. Iqbal, M. Shafiq, Z.R. Farooqi, A. Shah, W. Khan, Impacts of anthropogenic activities & climate change resulting from increasing concentration of carbon dioxide on environment in 21st century; a critical review, IOP Conf. Ser. Earth Environ. Sci. 1194 (2023) 012010, https://doi.org/10.1088/1755-1315/1194/1/012010.

[2] L.J.R. Nunes, The rising threat of atmospheric CO2: a review on the causes, impacts, and mitigation strategies, Environments 10 (2023) 66, https://doi.org/10.3390/environments10040066.

[3] M.A. Shah, A.L. Shibiru, V. Kumar, V.C. Srivastava, Carbon dioxide conversion to value-added products and fuels: opportunities and challenges: a critical review, Int. J. Green. Energy (2023). ⟨https://www.tandfonline.com/doi/abs/10.1080/15435075.2023.2281330⟩ (accessed November 17, 2024).

[4] G. Yergaziyeva, Z. Kuspanov, M. Mambetova, N. Khudaibergenov, N. Makayeva, C. Daulbayev, Advancements in catalytic, photocatalytic, and electrocatalytic CO2 conversion processes: current trends and future outlook, J. CO2 Util. 80 (2024) 102682, https://doi.org/10.1016/j.jcou.2024.102682.

[5] U. Kanivets, G. Murzagalina, N. Prodanova, N. Gavrilieva, Reducing the risks of anthropogenic impact on the environment in the light of the concept of sustainable development, E3S Web Conf. 389 (2023) 02011, https://doi.org/10.1051/e3sconf/202338902011.

[6] J. Huang, Q. Liu, J. Huang, M. Xu, W. Lai, Z. Gu, Electrochemical CO2 reduction to multicarbon products on non-copper based catalysts, ChemSusChem (2024) e202401173, https://doi.org/10.1002/cssc.202401173.

[7] X. Jiang, R. Chen, Y.-X. Chen, C.-Z. Lu, Research progress of photoelectrochemical conversion of CO_2 to C_{2+} products, Chem. Synth. 4 (2024), https://doi.org/10.20517/cs.2024.03.

[8] H.-R. "Molly" Jhong, S. Ma, P.J. Kenis, Electrochemical conversion of CO2 to useful chemicals: current status, remaining challenges, and future opportunities, Curr. Opin. Chem. Eng. 2 (2013) 191–199, https://doi.org/10.1016/j.coche.2013.03.005.

[9] T. Baran, M. Aresta, R. Comparelli, A. Dibenedetto, Gas-Phase photocatalytic coprocessing of CO2 – H2O(v) to energy products promoted by the n,n-Junction In2O3@g-C3N4 under VIS-Light, ChemSusChem (2024) e202400661, https://doi.org/10.1002/cssc.202400661.

[10] J.-J. Velasco-Vélez, A. Knop-Gericke, B. Roldan-Cuenya, R. Schlögl, T.E. Jones, Pseudocapacitance facilitates the electrocatalytic reduction of carbon dioxide, Adv. Energy Mater. 14 (2024) 2400054, https://doi.org/10.1002/aenm.202400054.

[11] M. Jiang, H. Wang, M. Zhu, X. Luo, Y. He, M. Wang, C. Wu, L. Zhang, X. Li, X. Liao, Z. Jiang, Z. Jin, Review on strategies for improving the added value and expanding the scope of CO2 electroreduction products, Chem. Soc. Rev. 53 (2024) 5149–5189, https://doi.org/10.1039/D3CS00857F.

[12] A.J. King, J.C. Bui, C. Kim, W. Wei, K.-H. Kim, J. Safipour, A. Kusoglu, F.M. Toma, A.T. Bell, A.Z. Weber, Invited) exploring Solar-Driven CO2 reduction to C2+ products, Meet. Abstr. (2023) 2361, https://doi.org/10.1149/MA2023-02472361mtgabs.

[13] Y. Sun, Z. Luo, J. Qiu, Breakthrough in CO2 electroreduction to multi-carbon products at Ampere-Level enabled by active sites engineering, Angew. Chem. Int. Ed. 63 (2024) e202406879, https://doi.org/10.1002/anie.202406879.

[14] W.Q. Chen, J.L.C. Foo, L.Y. Ge, A. Veksha, W.-P. Chan, Y. Shen, G. Lisak, Electrocatalytic reduction of simulated industrial CO2 and CO mixtures: revising chronoamperometry to enable selective gas mixture reduction via cyclic voltammetry, Chem. Eng. J. 487 (2024) 150602, https://doi.org/10.1016/j.cej.2024.150602.

[15] J. Antonio Abarca, G. Díaz-Sainz, I. Merino-Garcia, A. Irabien, J. Albo, Photoelectrochemical CO2 electrolyzers: from photoelectrode fabrication to reactor configuration, J. Energy Chem. 85 (2023) 455–480, https://doi.org/10.1016/j.jechem.2023.06.032.

[16] J.H. Kim, S.H. Hong, S.H. Ahn, S.Y. Kim, Recent progress in photocathode interface engineering for photoelectrochemical CO2 reduction reaction to C1 and C2+ products, Authorea (2024), https://doi.org/10.22541/au.171249329.92633049/v1.

[17] I. Merino-Garcia, J. Albo, J. Solla-Gullón, V. Montiel, A. Irabien, Cu oxide/ZnO-based surfaces for a selective ethylene production from gas-phase CO2 electroconversion, J. CO2 Util. 31 (2019) 135–142, https://doi.org/10.1016/j.jcou.2019.03.002.

[18] Y. Liu, M. Xia, D. Ren, S. Nussbaum, J.-H. Yum, M. Grätzel, N. Guijarro, K. Sivula, Photoelectrochemical CO2 reduction at a direct CuInGaS2/Electrolyte junction, ACS Energy Lett. 8 (2023) 1645–1651, https://doi.org/10.1021/acsenergylett.3c00022.

[19] J.H. Cho, J. Ma, S.Y. Kim, Toward high-efficiency photovoltaics-assisted electrochemical and photoelectrochemical CO2 reduction: strategy and challenge, Exploration 3 (2023) 20230001, https://doi.org/10.1002/EXP.20230001.

[20] K. Xu, Q. Zhang, X. Zhou, M. Zhu, H. Chen, Recent progress and perspectives on photocathode materials for CO2 catalytic reduction, Nanomaterials 13 (2023) 1683, https://doi.org/10.3390/nano13101683.

[21] K.M.K. Yap, S.-W. Lee, M.A. Steiner, J.E.A. Acosta, D. Kang, D. Kim, E.L. Warren, A.C. Nielander, T.F. Jaramillo, A framework for understanding efficient diurnal CO2 reduction using si and GaAs photocathodes, Chem. Catal. 3 (2023), https://doi.org/10.1016/j.checat.2023.100641.

[22] K. Lee, S. Lee, H. Cho, S.-E. Jeong, W.D. Kim, S. Lee, D.C. Lee, Cu + -incorporated TiO 2 overlayer on cu 2 o nanowire photocathodes for enhanced photoelectrochemical conversion of CO 2 to methanol, J. Energy Chem. 27 (2018) 264–270, https://doi.org/10.1016/J.JECHEM.2017.04.019.

[23] L. Talbi, I. Bozetine, S.A. Boussaa, K. Benfadel, D. Allam, N. Rahim, Y. O. Mohamed, M. Leitgeb, C. Torki, S. Hocine, F. Boudeffar, A. Manseri, S. Kaci, Photoelectrochemical properties of Cu2O/PANI/Si-based photocathodes for CO2 conversion, Emerg. Mater. Res. 12 (2023) 78–91, https://doi.org/10.1680/jemmr.22.00167.

[24] N.H. Lam, N.T.N. Truong, N. Le, K.-S. Ahn, Y. Jo, C.-D. Kim, J.H. Jung, Improving the photoelectrochemical water splitting performance of CuO photocathodes using a protective CuBi2O4 layer, Sci. Rep. 13 (2023) 5776, https://doi.org/10.1038/s41598-023-32804-0.

[25] A. Zindrou, L. Belles, Y. Deligiannakis, Cu-Based materials as photocatalysts for solar light artificial photosynthesis: aspects of engineering performance, stability, selectivity, Solar 3 (2023) 87–112, https://doi.org/10.3390/solar3010008.

[26] G. Solomon, M. Lecca, M. Bisetto, M. Gilzad Kohan, I. Concina, M.M. Natile, A. Vomiero, Engineering Cu2O nanowire surfaces for photoelectrochemical hydrogen evolution reaction, ACS Appl. Energy Mater. 6 (2023) 832–840, https://doi.org/10.1021/acsaem.2c03122.

[27] N. Hoang Lam, N. Tam Nguyen Truong, K.-S. Ahn, Y. Jo, S. Beom Kang, N. Huu Hieu, S.F. Shaikh, C.-D. Kim, M. Lee, J. Hak Jung, CuO photocathode enhancement through ultra-thin carbon coating layer for photoelectrochemical water splitting, FlatChem 43 (2024) 100600, https://doi.org/10.1016/j.flatc.2023.100600.

[28] M. Patel, H.-S. Kim, D.B. Patel, J. Kim, CuO photocathode-embedded semitransparent photoelectrochemical cell, J. Mater. Res. 31 (2016) 3205–3213, https://doi.org/10.1557/jmr.2016.364.

[29] M. Zhang, W. Luo, S. Gu, W. Xu, Z. Lu, F. Wang, Photoelectrochemical catalytic CO2 reduction enhanced by In-doped GaN and combined with vibration energy harvester driving CO2 reduction, Appl. Catal. A Gen. 683 (2024) 119859, https://doi.org/10.1016/j.apcata.2024.119859.

[30] X. Zhang, J. Wang, Y. Liu, J. Sun, B. Xu, T. Li, Photoelectrocatalytic reduction of CO2 to CO via Cu2O/C/PTFE nanowires photocathodes, ChemPhotoChem 8 (2024) e202400005, https://doi.org/10.1002/cptc.202400005.

[31] Y. Chen, C. Xiang, M. Lin, Performance assessment of photoelectrochemical CO2 reduction photocathodes with patterned electrocatalysts: a multi-physical model-based approach, Energy Environ. Sci. 17 (2024) 3032–3041, https://doi.org/10.1039/D4EE00575A.

[32] A.K. Singh, J.H. Montoya, J.M. Gregoire, K.A. Persson, Robust and synthesizable photocatalysts for CO2 reduction: a data-driven materials discovery, Nat. Commun. 10 (2019) 443, https://doi.org/10.1038/s41467-019-08356-1.

[33] R. Kumar, J. Kaur, M. Rawat, A.A. Alarfaj, R. Acevedo, M. Cascione, V. De Matteis, J. Singh, Biogenic synthesis of CuO nanoparticles for efficient photocatalytic degradation of industrial pollutants, Hum. Ecol. Risk Assess. Int. J. 29 (2023) 927–937, https://doi.org/10.1080/10807039.2023.2210223.

[34] S. Tyagi, A. Kumar, P.K. Tyagi, M. Hatami, Development and characterization of biogenic copper oxide nanoparticles, with an exploration of their antibacterial and antioxidant potential, 3 Biotech 14 (2024) 20, https://doi.org/10.1007/s13205-023-03869-5.

[35] A. Waris, M. Din, A. Ali, M. Ali, S. Afridi, A. Baset, A. Ullah Khan, A comprehensive review of Green synthesis of copper oxide nanoparticles and their diverse biomedical applications, Inorg. Chem. Commun. 123 (2021) 108369, https://doi.org/10.1016/j.inoche.2020.108369.

[36] D. Gupta, A. Boora, A. Thakur, T.K. Gupta, Green and sustainable synthesis of nanomaterials: recent advancements and limitations, Environ. Res. 231 (2023) 116316, https://doi.org/10.1016/j.envres.2023.116316.

[37] M.C. Ogwuegbu, A.S. Ayangbenro, D.M.N. Mthiyane, O.O. Babalola, D. C. Onwudiwe, Green synthesis of CuO nanoparticles using ligustrum lucidum extract, and the antioxidant and antifungal evaluation, Mater. Res. Express 11 (2024) 055010, https://doi.org/10.1088/2053-1591/ad4e9d.

[38] A. Pawar, A. Mungole, K. Naktode, Biogenic copper oxide nanoparticles synthesized from whole plant extract of nicotiana plumbaginifolia viv.: characterization, antibacterial, and antioxidant properties, J. Turk. Chem. Soc. Sec. A 11 (2024) 1005–1016, https://doi.org/10.18596/jotcsa.1422924.

[39] T. Ferreira-Gonçalves, M.M. Gaspar, J.M.P. Coelho, V. Marques, A.S. Viana, L. Ascensão, L. Carvalho, C.M.P. Rodrigues, H.A. Ferreira, D. Ferreira, C.P. Reis, The role of rosmarinic acid on the bioproduction of gold nanoparticles as part of a photothermal approach for breast cancer treatment, Biomolecules 12 (2022) 71, https://doi.org/10.3390/biom12010071.

[40] S.H. Lim, Y. Park, Green synthesis, characterization and catalytic activity of gold nanoparticles prepared using rosmarinic acid, J. Nanosci. Nanotechnol. 18 (2018) 659–667, https://doi.org/10.1166/jnn.2018.13982.

[41] M. Kalaiyarasi, M. Nivedha, M. Mani, R. Harikrishnan, J.K. Kumar, S. Loganathan, K. Kaviyarasu, Synthesis of CuO/NaCuSO4 nanocomposite using an aqueous extract of tribulus terrestris and their structural, optical, morphology and dielectric studies, Chem. Pap. 78 (2024) 3083–3098, https://doi.org/10.1007/s11696-023-03294-1.

[42] A. Mrabet, B. Abdelfattah, F. El Mansouri, A. Simou, M. Khaddor, Bay laurel of Northern Morocco: a comprehensive analysis of its phytochemical profile, mineralogical composition, and antioxidant potential, Biophysica 4 (2024) 238–255, https://doi.org/10.3390/biophysica4020017.

[43] M. Khandelwal, S. Choudhary, Harish, A. Kumawat, K.P. Misra, Y. Vyas, B. Singh, D.S. Rathore, K. Soni, A. Bagaria, R.K. Khangarot, An Eco-Friendly synthesis approach for enhanced photocatalytic and antibacterial properties of copper oxide nanoparticles using Coelastrella terrestris algal extract, Int. J. Nanomed. 19 (2024) 4137–4162, https://doi.org/10.2147/IJN.S452889.

[44] A. Mrabet, H. Annaz, B. Abdelfattah, M. Ouabou, A. Kounnoun, F. Cacciola, A. Simou, N. Bouayad, K. Rharrabe, M. Khaddor, Antioxidant, insecticidal, antifeedant, and repellent activities of oregano (*origanum vulgare*), Int. J. Environ. Health Res. (2024) 1–16, https://doi.org/10.1080/09603123.2024.2355292.

[45] P. Kaushal, D. Maity, R. Awasthi, Nano-Green: harnessing the potential of plant extracts for sustainable antimicrobial metallic nanoparticles, J. Drug Deliv. Sci. Technol. 94 (2024) 105488, https://doi.org/10.1016/j.jddst.2024.105488.

[46] A. Saloki, S.J. Daharwal, Green synthesis of copper oxide nanoparticle from plant extract and its antibacterial activity, Asian J. Pharm. Clin. Res. (2023) 172–176, https://doi.org/10.22159/ajpcr.2023.v16i7.47122.

[47] R.I. Mahmood, H.S. Mohammed-Salih, A. Ghazi, H.J. Abdulbaqi, J.R. Al-Obaidi, Exploring the potential of copper oxide biogenic synthesis: a review article on the biomedical and dental implementations, Arab Gulf J. Sci. Res. 42 (2023) 370–387, https://doi.org/10.1108/AGJSR-12-2022-0315.

[48] S. Dhir, R. Verma, S. Bhatt, V. Garg, R. Dutt, Green synthesis, characterization, and biomedical applications of copper and copper oxide nanoparticles of plant origin, Curr. Drug Ther. 18 (2023) 391–406, https://doi.org/10.2174/1574885518666230328150208.

[49] M. Singh, M. Changmai, T. Ghosh, A. Karwa, Natural Resource-Based nanobiomaterials. Advanced Materials and Manufacturing Techniques for Biomedical Applications, John Wiley & Sons, Ltd, 2023, pp. 61–101, https://doi.org/10.1002/9781394166985.ch4.

[50] H.M. Abuzeid, C.M. Julien, L. Zhu, A.M. Hashem, Green synthesis of nanoparticles and their energy storage, environmental, and biomedical applications, Crystals 13 (2023) 1576, https://doi.org/10.3390/cryst13111576.

[51] R. Agarwal, K. Verma, N.K. Agrawal, R.K. Duchaniya, R. Singh, Synthesis, characterization, thermal conductivity and sensitivity of CuO nanofluids, Appl. Therm. Eng. 102 (2016) 1024–1036, https://doi.org/10.1016/j.applthermaleng.2016.04.051.

[52] S. Chakkour, E. Bergmeier, S. Meyer, J. Kassout, M. Kadiri, M. Ater, Plant diversity in traditional agroecosystems of north Morocco, Veg. Classif. Surv. 4 (2023) 31–45, https://doi.org/10.3897/VCS.86024.

[53] K.R. Shubhashree, R. Reddy, A.K. Gangula, G.S. Nagananda, P.K. Badiya, S. S. Ramamurthy, P. Aramwit, N. Reddy, Green synthesis of copper nanoparticles using aqueous extracts from hyptis suaveolens (L.), Mater. Chem. Phys. 280 (2022) 125795, https://doi.org/10.1016/j.matchemphys.2022.125795.

[54] J.A. Abarca, G. Díaz-Sainz, I. Merino-Garcia, G. Beobide, J. Albo, A. Irabien, Optimized manufacturing of gas diffusion electrodes for CO2 electroreduction with automatic spray pyrolysis, J. Environ. Chem. Eng. 11 (2023) 109724, https://doi.org/10.1016/j.jece.2023.109724.

[55] Y. Zhao, I. Merino-Garcia, J. Albo, A. Kaiser, A Zero-Gap gas phase photoelectrolyzer for CO2 reduction with porous carbon supported photocathodes, ChemSusChem (2024), https://doi.org/10.1002/cssc.202400518.

[56] R. Sankar, P. Manikandan, V. Malarvizhi, T. Fathima, K.S. Shivashangari, V. Ravikumar, Green synthesis of colloidal copper oxide nanoparticles using *carica papaya* and its application in photocatalytic dye degradation, Spectrochim. Acta Part A Mol. Biomol. Spectrosc. 121 (2014) 746–750, https://doi.org/10.1016/j.saa.2013.12.020.

[57] A.S. Ethiraj, D.J. Kang, Synthesis and characterization of CuO nanowires by a simple wet chemical method, Nanoscale Res. Lett. 7 (2012) 70, https://doi.org/10.1186/1556-276X-7-70.

[58] B. Abdelfattah, A. Mrabet, A. Simou, M. Khaddor, Exploring the bioactive potential of cistus ladanifer leaves from Northern Morocco (Tangier), Ecol. Eng. Environ. Technol. 25 (2024) 316–330, https://doi.org/10.12912/27197050/187764.

[59] S. Shahzadi, S. Fatima, Q. Ul Ain, Z. Shafiq, M.R.S.A. Janjua, A review on Green synthesis of silver nanoparticles (SNPs) using plant extracts: a multifaceted approach in photocatalysis, environmental remediation, and biomedicine, RSC Adv. 15 (2025) 3858–3903, https://doi.org/10.1039/d4ra07519f.

[60] Z. Villagrán, L.M. Anaya-Esparza, C.A. Velázquez-Carriles, J.M. Silva-Jara, J. M. Ruvalcaba-Gómez, E.F. Aurora-Vigo, E. Rodríguez-Lafitte, N. Rodríguez-Barajas, I. Balderas-León, F. Martínez-Esquivias, Plant-Based extracts as reducing, capping, and stabilizing agents for the Green synthesis of inorganic nanoparticles, Resources 13 (2024) 70, https://doi.org/10.3390/resources13060070.

[61] K. Nakamoto. Infrared and Raman Spectra of Inorganic and Coordination Compounds: Part A: Theory and Applications in Inorganic Chemistry, 1st ed., Wiley, 2008 https://doi.org/10.1002/9780470405840.

[62] C. Vanlalveni, S. Lallianrawna, A. Biswas, M. Selvaraj, B. Changmai, S.L. Rokhum, Green synthesis of silver nanoparticles using plant extracts and their antimicrobial activities: a review of recent literature, RSC Adv. 11 (2021) 2804–2837, https://doi.org/10.1039/D0RA09941D.

[63] S.S. Shankar, A. Rai, A. Ahmad, M. Sastry, Rapid synthesis of au, ag, and bimetallic au core-Ag shell nanoparticles using neem (Azadirachta indica) leaf broth, J. Colloid Interface Sci. 275 (2004) 496–502, https://doi.org/10.1016/j.jcis.2004.03.003.

[64] L. Gontrani, E.M. Bauer, A. Talone, M. Missori, P. Imperatori, P. Tagliatesta, M. Carbone, CuO nanoparticles and microaggregates: an experimental and computational study of structure and electronic properties, Materials 16 (2023) 4800, https://doi.org/10.3390/ma16134800.

[65] M. Yadi, E. Mostafavi, B. Saleh, S. Davaran, I. Aliyeva, R. Khalilov, M. Nikzamir, N. Nikzamir, A. Akbarzadeh, Y. Panahi, M. Milani, Current developments in Green synthesis of metallic nanoparticles using plant extracts: a review, Artif. Cells Nanomed. Biotechnol. 46 (2018) 336–343, https://doi.org/10.1080/21691401.2018.1492931.

[66] Y.A. Dallatu, G.A. Shallangwa, S.N. Africa, Synthesis and growth of spherical ZnO nanoparticles using different amount of plant extract: characterization and morphology of structures, Jasem 24 (2021) 2147–2151, https://doi.org/10.4314/jasem.v24i12.21.

[67] S.-K. Kamaraj, Sustainable Green Synthesised Nano-dimensional Materials for Energy and Environmental Applications, First Edition, CRC Press/Taylor & Francis Group, Boca Raton, 2025.

[68] C. Espíndola, Some Nanocarrier's properties and chemical interaction mechanisms with flavones, Molecules 28 (2023) 2864, https://doi.org/10.3390/molecules28062864.

[69] R. Indiarto, L.P.A. Indriana, R. Andoyo, E. Subroto, B. Nurhadi, Bottom–up nanoparticle synthesis: a review of techniques, polyphenol-based core materials, and their properties, Eur. Food Res Technol. 248 (2022) 1–24, https://doi.org/10.1007/s00217-021-03867-y.

[70] C. Xu, G. Xu, M. Du, H. Zhu, Y. Fu, X. Zhang, Effects of plant polyphenols on the interface and mechanical properties of Rubber/Silica composites, Polym. Polym. Compos. 20 (2012) 853–860, https://doi.org/10.1177/096739111202000912.

[71] F. Behboodi-Sadabad, V. Trouillet, A. Welle, P.B. Messersmith, P.A. Levkin, Surface functionalization and patterning by multifunctional resorcinarenes, ACS Appl. Mater. Interfaces 10 (2018) 39268–39278, https://doi.org/10.1021/acsami.8b14771.

[72] A. George, D.M.A. Raj, A.D. Raj, B.-S. Nguyen, T.-P. Phan, T. Pazhanivel, K. Sivashanmugan, R.L. Josephine, A.A. Irudayaraj, J. Arumugam, V.-H. Nguyen, Morphologically tailored CuO nanostructures toward visible-light-driven photocatalysis, Mater. Lett. 281 (2020) 128603, https://doi.org/10.1016/j.matlet.2020.128603.

[73] J.-L. Ortiz-Quiñonez, U. Pal, Interface engineered metal oxide heterojunction nanostructures in photocatalytic CO2 reduction: progress and prospects, Coord. Chem. Rev. 516 (2024) 215967, https://doi.org/10.1016/j.ccr.2024.215967.

[74] M. Abouri, A. Benzaouak, F. Zaaboul, A. Sifou, M. Dahhou, M.A. El Belghiti, K. Azzaoui, B. Hammouti, L. Rhazi, R. Sabbahi, M.M. Alanazi, A. El Hamidi, Efficient catalytic reduction of organic pollutants using nanostructured CuO/TiO2 catalysts: synthesis, characterization, and reusability, Inorganics 12 (2024) 297, https://doi.org/10.3390/inorganics12110297.

[75] A.M.A. Al-Khazraji, E.J. Waheed, A.A.R. Ahmed, Synthesis of CuO nanoparticles from Copper(II) schiff base complex: evaluation via thermal decomposition, Indones. J. Chem. 25 (2025) 50, https://doi.org/10.22146/ijc.95427.

[76] S. Gates-Rector, T. Blanton, The powder diffraction file: a quality materials characterization database, Powder Diffr. 34 (2019) 352–360, https://doi.org/10.1017/S0885715619000812.

[77] S. Wojtyła, T. Baran, Electrochemically prepared copper/indium oxides photocathode for efficient photoelectrochemical hydrogen production, Sol. Energy Mater. Sol. Cells 206 (2020) 110262, https://doi.org/10.1016/j.solmat.2019.110262.

[78] T. Egerton, UV-Absorption—The primary process in photocatalysis and some practical consequences, Molecules 19 (2014) 18192–18214, https://doi.org/10.3390/molecules191118192.

[79] Z. Zhang, B. Zhu, X. Guan, Operational spectroelectrochemical investigation on the interfacial charge dynamics of copper bismuth oxide based photocathode, J. Phys. Chem. Lett. 13 (2022) 2356–2364, https://doi.org/10.1021/acs.jpclett.2c00140.

[80] P. Makuła, M. Pacia, W. Macyk, How to correctly determine the band gap energy of modified semiconductor photocatalysts based on UV–Vis spectra, J. Phys. Chem. Lett. 9 (2018) 6814–6817, https://doi.org/10.1021/acs.jpclett.8b02892.

[81] B.D. Viezbicke, S. Patel, B.E. Davis, D.P. Birnie, Evaluation of the tauc method for optical absorption edge determination: ZnO thin films as a model system, Phys. Status Solidi B 252 (2015) 1700–1710, https://doi.org/10.1002/pssb.201552007.

[82] D.K. Sarkar, V. Selvanathan, M. Mottakin, Md.A. Islam, H. Almohamadi, N. H. Alharthi, Md Akhtaruzzaman, Phytochemicals assisted Green synthesis of copper oxide/cobalt oxide as efficient electrocatalyst for oxygen evolution reaction, Int. J. Hydrog. Energy 51 (2024) 700–712, https://doi.org/10.1016/j.ijhydene.2023.07.042.

[83] Sandip P. GondakeDr. Shirish S. Pingale, Synthesis of metal oxide nanoparticles using Indian medicinal plants for photocatalytic applications - a review, Int. J. Sci. Res. Sci. Technol. (2022) 80–93, https://doi.org/10.32628/IJSRST2294101.

[84] H.N. Cuong, S. Pansambal, S. Ghotekar, R. Oza, N.T. Thanh Hai, N.M. Viet, V.-H. Nguyen, New frontiers in the plant extract mediated biosynthesis of copper oxide (CuO) nanoparticles and their potential applications: a review, Environ. Res. 203 (2022) 111858, https://doi.org/10.1016/j.envres.2021.111858.

[85] M.A. Abomuti, E.Y. Danish, A. Firoz, N. Hasan, M.A. Malik, Green synthesis of zinc oxide nanoparticles using salvia officinalis leaf extract and their photocatalytic and antifungal activities, Biology 10 (2021) 1075, https://doi.org/10.3390/biology10111075.

[86] F.U. Rehman, R. Mahmood, S. Haq, P. Ahmad, S.U. Din, M.U. Khandaker, A. M. Idris, I. Zekker, Phytogenic fabrication of copper oxide nanoparticles for antibacterial and antioxidant screening: physico-chemical study, Crystals 12 (2022) 1796, https://doi.org/10.3390/cryst12121796.

[87] V. Selvanathan, M. Aminuzzaman, L.-H. Tey, S.A. Razali, K. Althubeiti, H. I. Alkhammash, S.K. Guha, S. Ogawa, A. Watanabe, Md Shahiduzzaman, Md Akhtaruzzaman, Muntingia calabura leaves mediated green synthesis of CuO nanorods: exploiting phytochemicals for unique morphology, Materials 14 (2021) 6379, https://doi.org/10.3390/ma14216379.

[88] D.S. Zimbovskii, O. Kapitanova, X. Xu, G.N. Panin, A.N. Baranov, Cu_2 o photocathodes modified by graphene oxide and ZnO nanoparticles with improved photocatalytic properties, Langmuir 39 (2023) 18509–18517, https://doi.org/10.1021/acs.langmuir.3c02839.

[89] B. Ameri, S.S.H. Davarani, R. Roshani, H.R. Moazami, A. Tadjarodi, A flexible mechanochemical route for the synthesis of copper oxide nanorods/nanoparticles/nanowires for supercapacitor applications: the effect of morphology on the charge storage ability, J. Alloy. Compd. 695 (2017) 114–123, https://doi.org/10.1016/j.jallcom.2016.10.144.

[90] S.D. Kasi, J.M. Ramasamy, D. Nagaraj, V. Santiyagu, J.S. Ponraj, Biogenic synthesis of copper oxide nanoparticles using leaf extracts of *cissus quadrangularis* and *piper betle* and its antibacterial effects, micro &amp, Nano Lett. 16 (2021) 419–424, https://doi.org/10.1049/mna2.12066.

[91] H.-P. Feng, J.-Y. Lin, M.-Y. Cheng, Y.-Y. Wang, C.-C. Wan, Behavior of copper removal by CMP and its correlation to deposit structure and impurity content, J. Electrochem. Soc. 155 (2008) H21, https://doi.org/10.1149/1.2801394.

[92] S. Shiomi, Impurity-driven simultaneous size and crystallinity control of metal nanoparticles, Nanotechnology 34 (2023) 465604, https://doi.org/10.1088/1361-6528/acf04c.

[93] J. García-Melero, J.-J. López-Mitjavila, M.J. García-Celma, C. Rodriguez-Abreu, S. Grijalvo, Rosmarinic acid-loaded polymeric nanoparticles prepared by low-energy nano-emulsion templating: formulation, biophysical characterization, and in vitro studies, Materials 15 (2022) 4572, https://doi.org/10.3390/ma15134572.

[94] A. Sarkar, S.P. Shukla, S. Adhikari, T. Mukherjee, Synthesis, stabilisation and surface modification of gold and silver nanoparticles by rosmarinic acid and its analogues, Int. J. Nanotechnol. 7 (2010) 1027, https://doi.org/10.1504/IJNT.2010.034707.

[95] S. Iravani, Green synthesis of metal nanoparticles using plants, Green Chem. 13 (2011) 2638, https://doi.org/10.1039/c1gc15386b.

[96] J. Shi, X. Zhao, C. Li, Surface passivation engineering for photoelectrochemical water splitting, Catalysts 13 (2023) 217, https://doi.org/10.3390/catal13020217.

[97] M. Khandelwal, S. Choudhary, Harish, A. Kumawat, K.P. Misra, D.S. Rathore, R. K. Khangarot, Asterarcys quadricellulare algae-mediated copper oxide nanoparticles as a robust and recyclable catalyst for the degradation of noxious dyes from wastewater, RSC Adv. 13 (2023) 28179–28196, https://doi.org/10.1039/d3ra05254k.

[98] X. Deng, R. Li, S. Wu, L. Wang, J. Hu, J. Ma, W. Jiang, N. Zhang, X. Zheng, C. Gao, L. Wang, Q. Zhang, J. Zhu, Y. Xiong, Metal-organic framework coating enhances the performance of Cu2O in photoelectrochemical CO2 reduction, J. Am. Chem. Soc. (2019), https://doi.org/10.1021/jacs.9b06239.

[99] X. Jiang, X. Hu, M. Tarek, P. Saravanan, R. Alqadhi, S. Chin, M.R. Khan, Tailoring the properties of g-C3N4 with CuO for enhanced photoelectrocatalytic CO2 reduction to methanol, J. CO 2 Util. 40 (2020), https://doi.org/10.1016/j.jcou.2020.101222.

[100] Y. Zhang, W. Qiu, Y. Liu, K. Wang, W. Li, J. Kang, X. Qiu, M. Liu, W. Li, J. Li, Modulating the Cu2O Photoelectrode/Electrolyte interface with bilayer surfactant simulating cell membranes for boosting photoelectrochemical CO2 reduction, J. Phys. Chem. Lett. (2023) 6301–6308, https://doi.org/10.1021/acs.jpclett.3c00672.

[101] P. Uthirakumar, H. Son, V. Dao, Y. Lee, S. Yadav, I.-H. Lee, Accelerating photoelectrochemical CO2RR selectively of C2+ products by integrating Ag/Pd cocatalysts on Cu/Cu2O/CuO heterojunction nanorods, J. Environ. Chem. Eng. 12 (2024) 112442, https://doi.org/10.1016/j.jece.2024.112442.

[102] L. Talbi, I. Bozetine, S.A. Boussaa, K. Benfadel, D. Allam, N. Rahim, Y. O. Mohamed, M. Leitgeb, C. Torki, S. Hocine, F. Boudeffar, A. Manseri, S. Kaci, Photoelectrochemical properties of Cu2O/PANI/Si-based photocathodes for CO2 conversion, Emerg. Mater. Res. 12 (2023) 78–91, https://doi.org/10.1680/jemmr.22.00167.

[103] K.Md.R. Karim, M. Tarek, ShaheenM. Sarkar, R. Mouras, H.R. Ong, H. Abdullah, C.K. Cheng, Md.M.R. Khan, Photoelectrocatalytic reduction of CO2 to methanol over CuFe2O4@PANI photocathode, Int. J. Hydrog. Energy 46 (2021) 24709–24720, https://doi.org/10.1016/j.ijhydene.2020.02.195.

[104] S. Chu, X. Yan, C. Choi, S. Hong, A.W. Robertson, J. Masa, B. Han, Y. Jung, Z. Sun, Stabilization of cu+ by tuning a CuO–CeO2 interface for selective electrochemical CO2 reduction to ethylene, Green Chem. 22 (2020) 6540–6546, https://doi.org/10.1039/D0GC02279A.

[105] D. Chi, H. Yang, Y. Du, T. Lv, G. Sui, H. Wang, J. Lu, Morphology-controlled CuO nanoparticles for electroreduction of CO2 to ethanol, RSC Adv. 4 (2014) 37329–37332, https://doi.org/10.1039/C4RA05415F.

[106] F.T. Angerasa, E.A. Moges, C.-Y. Chang, K. Lakshmanan, T.A. Dessie, W.-H. Huang, H.G. Edao, W.B. Dilebo, C.B. Guta, C.-C. Chang, W.-S. Liao, J. Shen, N. G. Habtu, M.-C. Tsai, W.-N. Su, B.J. Hwang, Selective electrochemical reduction of CO_2 to ethanol on a heteroatom-coordinated dual-atom catalyst of Fe/Cu-NC, Chem. Mater. 37 (2025) 2474–2484, https://doi.org/10.1021/acs.chemmater.4c02803.

[107] J. Herranz, A.A. Permyakova, M. El Kazzi, M. Povia, A. Patru, T.J. Schmidt, Disclosing the oxidation state of copper oxides upon electrochemical CO_2-Reduction, Meet. Abstr. (2018), https://doi.org/10.1149/ma2018-02/54/1918.

[108] J. DuChene, G. Tagliabue, A. Welch, X. Li, W.-H. Cheng, H. Atwater, Optical excitation of a nanoparticle Cu/p-NiO photocathode improves reaction selectivity for CO2 reduction in aqueous electrolytes, Nano Lett. (2020), https://doi.org/10.1021/acs.nanolett.9b04895.

[109] K. Rajeshwar, N.R. de Tacconi, G. Ghadimkhani, W. Chanmanee, C. Janáky, Tailoring copper oxide semiconductor nanorod arrays for photoelectrochemical reduction of carbon dioxide to methanol, ChemPhysChem 14 (2013) 2251–2259, https://doi.org/10.1002/cphc.201300080.

[110] M. Xia, L. Pan, Y. Liu, J. Gao, J. Li, M. Mensi, K. Sivula, S.M. Zakeeruddin, D. Ren, M. Grätzel, Efficient Cu2O photocathodes for aqueous photoelectrochemical CO2 reduction to formate and syngas, J. Am. Chem. Soc. 145 (2023) 27939–27949, https://doi.org/10.1021/jacs.3c06146.